Selenium nanowire formation by reaction of selenate with magnetite

Poulain, A.; Fernandez-Martinez, A.; Greneche, J.-M.; Prieur, D.; Scheinost, A.; Menguy, N.; Bureau, S.; Magnin, V.; Findling, N.; Drnec, J.; Martens, I.; Mirolo, M.; Charlet, L.;

Originally published:

October 2022

Environmental Science & Technology 56(2022)20, 14817-14827

DOI: https://doi.org/10.1021/acs.est.1c08377

Selenium nanowire formation by reaction of selenate with magnetite

Journal:	*Environmental Science & Technology*
Manuscript ID	es-2021-083772
Manuscript Type:	Article
Date Submitted by the Author:	07-Dec-2021
Complete List of Authors:	Poulain, Agnieszka; ISTerre, Univ. Grenoble Alpes, Univ. Savoie Mont Blanc, CNRS, IRD, IFSTTAR Fernandez-Martinez, Alejandro; CNRS, ISTerre Greneche, Jean-Marc; Institut des Molécules et Matériaux du Mans Prieur, Damien; ESRF Scheinost, Andreas; The Rossendorf Beamline (BM20), European Synchrotron Radiation Lab Menguy, Nicolas; Sorbonne Université, IMPMC - UMR CNRS 7590 Bureau, Sarah; ISTerre Magnin, Valerie; ISTerre Findling, Nathaniel; ISTerre Drnec, Jakub; ESRF Martens, Isaac; ESRF Mirolo, Marta; ESRF, Experimental Charlet, Laurent; Institut des Sciences de la Terre,

Selenium nanowire formation by reaction of selenate with magnetite

Agnieszka Poulain[1], Alejandro Fernandez-Martinez[1], Jean-Marc Greneche[2], Damien Prieur[3], Andreas C. Scheinost[3], Nicolas Menguy[4], Sarah Bureau[1], Valérie Magnin[1], Nathaniel Findling[1], Jakub Drnec[5], Isaac Martens[5], Marta Mirolo[5], Laurent Charlet[1*]*

[1] Univ. Grenoble Alpes, Univ. Savoie Mont Blanc, CNRS, IRD, IFSTTAR, ISTerre, 38000 Grenoble, France

[2] Institut des Molécules et Matériaux du Mans, CNRS UMR-6283, Le Mans Université, Le Mans, F-72085, France.

[3] The Rossendorf Beamline at ESRF, 71 avenue des Martyrs, 38043 Grenoble, France, and HZDR Institute of Resource Ecology, Bautzener Landstrasse 400, 01328 Dresden, Germany

[4] Sorbonne Université, Muséum National d'Histoire Naturelle, UMR CNRS 7590, IRD. Institut de Minéralogie, de Physique des Matériaux et de Cosmochimie (IMPMC), 4 Place Jussieu, 75005, Paris, France

[5] ESRF, 71 avenue des Martyrs, 38043 Grenoble, France

KEYWORDS: Nuclear wastes, Selenium reduction, Sorption on magnetite, Selenium needles, Magnetite to maghemite interconversion

SYNOPSIS

Studies of selenate reduction on magnetite at neutral and acidic pH revealing different mechanism of radionuclide retention.

GRAPHICAL ABSTRACT

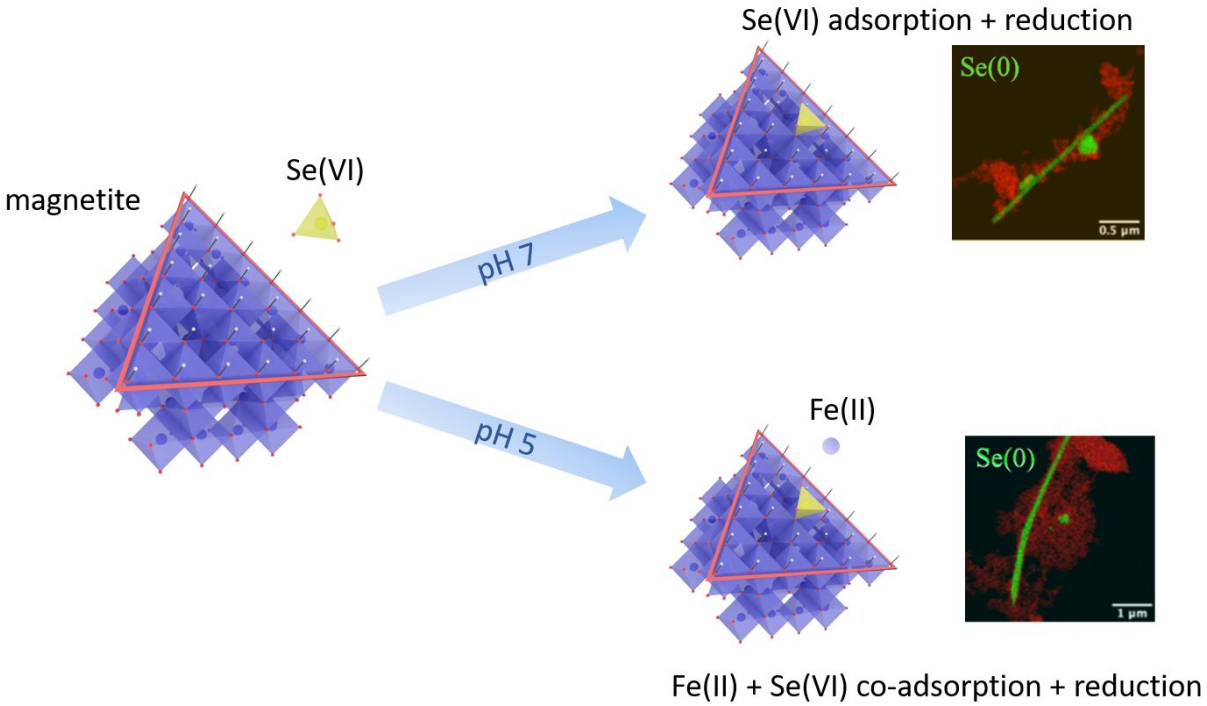

ABSTRACT

The mobility of ^{79}Se, a long half-life radioisotope and fission product of ^{235}U, and contaminant of drainage waters from black shale mountains and from coal mines, is an important parameter in the safety assessment of radioactive nuclear waste disposal systems. Highly mobile and soluble in its high oxidation states ($Se(VI)O_4^{2-}$, $Se(IV)O_3^{2-}$), selenium oxyanions can interact with magnetite, a mineral present in anoxic natural environments and in steel corrosion products, and be precipitated by reduction, and thus immobilized. Here, the sorption and reduction capacity of synthetic nanomagnetite towards Se(VI) was investigated at neutral and acidic pH, under reducing, oxygen free conditions. The additional presence of $Fe(II)_{aq}$, released during magnetite dissolution at pH 5, is shown to have an effect on the reduction kinetics. XANES analyses revealed that, at pH 5, trigonal gray Se(0) formed, and that outer-sphere Se(IV) complexes existed at the nanoparticle surface at longer reaction times. The Se(0) nanowires grew during the reaction, which points to a complex transport mechanism of reduced species or to active reduction sites at the tip of the Se(0) nanowires. The concomitant uptake of aqueous Fe(II) and Se(VI) ions is interpreted as a consequence of small pH oscillations that result from the Se(VI) reduction, leading to a re-adsorption of aqueous Fe(II) onto the magnetite, renewing its reducing capacity. This effect is not observed at pH 7, indicating that the presence of aqueous Fe(II) may be an important factor to be considered when examining the environmental reactivity of magnetite.

INTRODUCTION

Selenium is an essential micronutrient often called 'double-edged sword element'[1] or 'essential toxin',[2] due to one of the narrowest tolerance limits (40 and 400 μg/day).[3-4] Its maximum allowed concentration in drinking water has been set to 50 μg/L (US Environmental Protection Agency) and 40 μg/L (World Health Organization). Aqueous species of selenium show a variety of oxidation states, the distribution of which depends strongly on the environmental conditions. Selenate ($Se(VI)O_4^{2-}$) and selenite ($Se(IV)O_3^{2-}$) are water-soluble species which account for 95 % of selenium toxicity related to accumulation in plant and animal tissues,[3] reflecting its concentration and bioavailability in soils. Se(VI) predominates at high redox potential and under alkaline conditions and has a low adsorption and precipitation ability, while Se(IV) occurs at moderate redox potentials and its mobility is mainly governed by sorption/desorption processes.[4] Elemental selenium [Se(0)], metals selenides [Se(-II) and Se(-I)] and selenium sulfides are essentially insoluble and thus immobile in soils, hence selenium reduction strategies are used in decontamination technologies.[5] The reduced forms predominate under strongly reducing and acidic conditions with high amounts of organic matter.

While selenium-deficient environments are much more common than seleniferous environments, high natural concentrations are associated with crustal weathering of organic-rich shales, coals, volcanic activity and sulfidic mineralization, and phosphate rocks.[6] For example an urban development of a historical wetland in Upper Newport Bay, US[7] brought watershed contamination related to weathering of pyrite bearing black shale[8] flushing out from the vadose zone down to Newport Bay with large impact on its bird wildlife.[9] Point pollution is usually associated with human activity including coal and oil combustion facilities,[10] selenium refining factories, non-

ferrous metal smelting and refining factories,[11] mining,[12] manufacturing and utilization of agriculture products, irrigation,[13] flint soda-lime-silica glass production[14-15] and nuclear waste disposal. These industrial effluents often exceed the selenium drinking water limits by 10-100 times.[12,16-17] Such anthropogenic emissions result in contamination at a regional scale of an otherwise selenium deficient environment.

The ^{79}Se radioisotope (half-life 2.95 x 10^5 years) is a ^{235}U fission product, which may affect the total cumulative dose of radioactivity by an eventual release from waste repositories to the biosphere.[18] Programs for radioactive waste storage focus nowadays on materials with high radionuclide (RN) retention capacities. For example, clay-mineral rich formations show low permeability and high capacity to retard the diffusion of most RNs in their cationic forms via sorption processes, but are less effective to retard the migration of anions like selenate and selenite.[19] Some nuclear glasses, e.g. the French ones, contain up to 0.04% total selenium by weight, with a Se(VI) species fraction ranging from 0.05% to 20%, depending on f_{O2} during the glass production process.

This highly mobile, long half-life selenium ion can be reductively precipitated in complex redox reactions initiated at corroding steel waste canisters, surrounding compacted clay liners, and in deep anoxic aquifers.[20-22] Abiotic reduction of soluble selenium species by Fe(II)-bearing materials (potential corrosion products) has been observed for several minerals such as green rust,[23-25] magnetite,[26-28] mackinawite and siderite,[27] pyrite,[29,30] troillite[31] and Fe(0).[32] The mixed-valence Fe(II)/(III) oxide magnetite (Fe_3O_4) shows a high redox reactivity towards selenium species.[26-28] Fe(II) desorb from magnetite at pH < 7 and has been shown to remain in solution and act as a

reactive species when in close contact with the surface.[33-35] As such, the presence of aqueous Fe(II) is an interesting parameter that needs to be further investigated to correctly assess the reactivity of different mixed-valence oxides towards selenium oxyanions.

The aim of this paper is to investigate sorption and reducing capacity of synthetic nanomagnetite towards Se(VI), in the reducing, oxygen free environment at neutral and acidic pH. A recent study by our group reported the reduction of selenite to elemental selenium by magnetite nanoparticles, but the kinetics of the process as well as the influence of Fe(II) were not investigated.[26] Here, the combination of two spectroscopy techniques helped to elucidate the redox mechanism: ^{57}Fe Mössbauer spectrometry was used to quantify Fe(II)/Fe(III) and hence magnetite to maghemite ratio, while K-edge X-ray Near-Edge spectroscopy (XANES) revealed oxidation states of Se adsorbed on solid samples. X-Ray Diffraction (XRD) patterns confirmed the mineral oxidation and presence of reduced crystalline Se form. Finally, Transmission Electron Microscopy (TEM) analyses of the reacted mineral enabled examination of the morphology and size of the magnetite particles and Se crystals.

MATERIALS AND METHODS

All solutions were prepared with boiled, nitrogen-degassed Millipore 18.2 MΩ water. Reagent grade NaOH (≥98 %, Sigma Aldrich) and HCl (37 %, Carl Roth) were used for preparation of 1 M and 0.1 M stock solutions for pH control. A SENTRON pH meter was calibrated with VWR buffers, and Pt redox electrode for Eh measurements with a 200 mV buffer solution. All

experiments and synthesis were conducted at room temperature in an Ar-filled Jacomex glovebox, with a controlled oxygen partial pressure (< 2 ppm).

Magnetite synthesis and characterization

Magnetite was synthesized following original protocol of Jolivet et al.[36] 60 ml of 6 M NH_3 (Sigma Aldrich) was slowly added to 50 ml solution containing [Fe_{tot}] = 0.55 M and [Fe(II)]/[Fe(III)] = 0.5, prepared by adding 0.4 M $FeCl_2$ (tetrahydrate, Sigma Aldrich) to 0.8 M $FeCl_3$ (hexahydrate, Merck). The solution turned black immediately upon mixing and was left for 24 h on a rotary shaker. Afterwards a strong magnet was used to separate the magnetic particles and the supernatant was filtered (0.22 μm MF-Millipore). Magnetite was rinsed 4 times with water and 2 times with 0.1 mM NaCl solution, the latter one also used for the magnetite storage.

XRD. Samples were loaded inside the glove box into kapton capillaries, sealed with epoxy glue and stored in anoxic conditions until measurement. X-ray powder diffraction data were collected at room temperature at the ID31 beamline at the ESRF (λ = 0.1907 Å) using a Pilatus3 X CdTe 2M detector with 172 μm × 172 μm pixel size. The detector calibration was done using NIST certified CeO_2 674b standard. Azimuthal integrations were performed using the pyFAI package.[37] The lattice parameters, average crystallite sizes from Debye-Scherrer equation and phase fractions were calculated using Rietveld analysis with the FullProf Suite.[38] The advantages of synchrotron over laboratory X-ray source are: a better signal to noise ratio thanks to high photon flux and noise-free detector (Figure S1), faster measurements (few seconds *vs* few hours) and the smaller amount of powder required (beneficial for small-scale sorption experiments).

BET. The specific surface area (SSA) was determined by the Brunauer−Emmett−Teller adsorption method (BET-N_2) at 77 K, using a Belsorp-Max (Bel Japan) volumetric gas sorption instrument. A small amount (0.418 g) of magnetite was loaded in a glass cell inside the glovebox and then dried under vacuum at 80 °C during 12 h. The SSA was calculated from the BET equation in the P/P_0 range 0.052-0.307.

^{57}Fe Mössbauer. The spectra were collected at 300 and 77 K using a conventional constant acceleration transmission spectrometer with a ^{57}Co(Rh) source and an α-Fe foil as calibration sample. To obtain 5 mg Fe/cm^2 to satisfy the fine absorber conditions, 20 mg of the powder was loaded inside the glovebox in flat round plastic holders, sealed with epoxy glue, and transported in oxygen free conditions. The hyperfine structure was modeled by means of quadrupole doublets and/or magnetic sextets with lorentzian lines using the homemade program MOSFIT.[39]

TEM. A few milligrams of solid samples were placed in plastic tubes, filled with 10 mL of ethanol (previously stored for several weeks in the glovebox), sealed with parafilm, and removed from the glovebox for 5 minutes for redistribution in an ultrasonic bath. Next, the solutions were immediately transferred back to the glovebox, diluted with ethanol to a barely distinguishable black color and drop-casted on pure carbon, 200 mesh Cu TEM grids (TED PELLA, INC.). The samples were transferred to the microscope in anoxic conditions and were in contact with air only for few minutes during mounting on the microscope sample holder. Conventional Transmission Electron Microscopy (TEM), High Angular Angle Dark Field imaging in scanning mode (STEM-HAADF), X-ray energy-dispersive spectroscopy (XEDS) and Selected Area Electron Diffraction (SAED) patterns were collected at IMPMC, Sorbonne University, Paris, using a JEOL 2100F

microscope. Fast Fourier Transform on HR TEM images were carried out using ImageJ software (https://imagej.nih.gov/ij/) and SAED pattern were indexed using SingleCrystal Software (http://www.crystalmaker.com/singlecrystal/index.html).

Batch sorption experiments

Sorption experiments of $Se(VI)O_4^{2-}$ on magnetite were performed in glass bottles at room temperature in an Ar-filled glovebox. The concentration of dry magnetite in four batches was fixed at 10 g/L in 0.1 mM NaCl background electrolyte. Due to stronger selenium adsorption on magnetite in acidic conditions,[26] pH 5 and 7 were selected for comparison. The acidity of the initial suspensions was adjusted during 4 days by adding HCl or NaOH stock solutions, until the pH was not drifting from the desired value more than 0.2 unit within 24h. At the end of equilibration, aliquots of Se(VI) stock solution were added to obtain the total target RN concentration equal to 8.6 mM (details in Table 1). This should cover 100% of the [-Fe-OH] surface reactive sites, as calculated from the BET-determined specific surface area values and the magnetite theoretical crystallographic site density of 8 sites/nm^2.[40]

The addition of the Se(VI) to magnetite suspension stabilized at pH 5 (*Se(VI)_pH5*) resulted in an increase of the pH to 5.4, which was immediately readjusted. No change of pH was observed upon addition of Se(VI) to the magnetite suspension stabilized at pH 7 (*Se(VI)_pH7*). The pH of the suspensions was monitored and readjusted, if necessary, throughout the experiment. The two reactors were placed on a rotary shaker and 5 ml aliquots of the suspension were sampled at selected time intervals. The solid was isolated by magnetic separation, dried using vacuum

filtration system (0.22 μm), and left for further XAS, Mössbauer spectroscopy, TEM, XRD characterization. The liquid was filtered through a syringe filter (0.22 μm) and left for ICP-AES, IC and Eh analysis.

ICP-AES and **IC**. The total concentrations of Se in the liquid samples were determined after dilution by ICP-AES (Varian 720ES, detection range 0.05 - 50 ppm), while the concentrations of Se(VI) and Se(IV) by Ion Chromatography (Dionex Inegrion HPIC, Thermo Scientific, detection range 0.1 - 10 ppm). Difference between the initial selenium content (c_0) and the measured value (c_e) provided the amount of adsorbed species.

XAS. Pelletized samples (BN filler) were transported and kept in a liquid Nitrogen dewar until the measurements in a closed-cycle He cryostat with He atmosphere at 15 K, to avoid photon-induced oxidation and to exclude thermal disorder. X-ray Absorption Spectra were collected at the Rossendorf Beamline (BM20)[41] at the ESRF, in fluorescence mode at the Se-K edge (12 657 eV), using a pair of Rh-coated mirrors for suppression of higher harmonics The energy of the Si(111) monochromator was calibrated using Au foil at L3 edge (11 918 keV). Fluorescence spectra were acquired with an 18-element solid-state Germanium detector (Ultra-LEGe, GUL0055, Mirion Technologies). Several spectra were measured to obtain sufficient signal quality. Energy calibration and merging of individual scans was performed with SixPack,[42] normalization of XANES spectra was done with WinXAS.[43] Derivation of the number of spectral components in the complete data, their identification set as well as determination of their fractions in individual samples was done with ITFA ,[44-45] using spectra of selenium standards.

RESULTS AND DISCUSSION

Magnetite characterization before sorption experiments

Magnetite (Fe_3O_4) and maghemite (γ-Fe_2O_3) have a similar inverse spinel structure with comparable unit cell parameters of 8.3963 Å and 8.347 Å in the microcrystalline state,[46-47] difficult to differentiate by laboratory XRD. Magnetite contains both Fe^{2+} (in octahedral sites) and Fe^{3+} cations (in tetrahedral and octahedral sites), while maghemite is an oxidized form of spinel, containing only Fe^{3+} cations in the two types of sites. This leads to unit cell shrinking due to both the smaller size of the Fe^{3+} cation in relation to Fe^{2+}, and the formation of cationic vacancies necessary to maintain charge balance. Because of possible deviations from perfect magnetite stoichiometry corresponding to an $Fe^{2+}/Fe^{3+} = 0.5$, a whole range of mixed phases is possible ($Fe^{2+}/Fe^{3+} = 0$ for pure maghemite).[48-49]

Although phase identification by laboratory XRD is challenging, due to nearly identical contribution of the crystallographic planes, it is still feasible.[48,50] Several XRD patterns measured using laboratory device (Bruker D8) and synchrotron X-rays confirmed that the synthesized magnetite that was kept in the glovebox, as well as stabilized at pH ≥ 7, represented the pure phase with $Fe^{2+}/Fe^{3} = 0.5$ and $a = 8.39$ Å (Figure S1). The average crystallite size of 15 nm was estimated using the Scherrer equation, while TEM image showed rather large distribution of particles ranging from 5 to 50 nm, aggregated in large clusters (Figure S2).

A typical Mössbauer spectrum of microcrystalline magnetite at room temperature consists of two magnetic sextets, one due to Fe^{3+} in tetrahedral positions and the other one due to Fe^{3+} and Fe^{2+} in

octahedral positions, which are averaged as $Fe^{2.5+}$ because of fast electron exchange above the Verwey transition at about 125 K. The ratio between $Fe^{3+}/Fe^{2.5+}$ is equal to ½.[53] On the other hand at 77 K, the spectrum differs from that at room temperature due to the Verwey transition observed at about 119 K, below which electron hopping is absent and the hyperfine structure must be described by means of the superposition of different magnetic sextets. A structural change from cubic (300 K) to monoclinic (77 K) phase can be best fitted with three to five sextets.[54-55] In the case of microcrystalline maghemite, the Mössbauer spectra consist of one magnetic sextet at temperatures below its magnetic ordering temperature T_N, which must be described by means of two magnetic components attributed to Fe^{3+} species, according to the values of isomer shift, located in tetrahedral and octahedral positions. Therefore, the stoichiometry of magnetite can be accurately estimated by Mössbauer measurements, which allow the Fe^{2+}/Fe^{3+} ratio to be successfully determined from the least square data fitting, particularly from the mean value of the isomer shift.[51-52,56--57]

In the present study, the Mössbauer spectrum of the "pure" magnetite at 300K (Figure S3, left) differs from the typical one, and shows broadened lines due to superparamagnetic relaxation effects due to the presence of nanoparticles.

Stabilization of the background electrolyte at pH 5

Lowering the pH of the suspension consisting of only background electrolyte and magnetite, prior to sorption experiments, brought substantial changes to the solid and liquid phases. As the iron concentration at t_0 in the following sorption experiments was accidentally not measured (first point

at 10 min) an additional experimental runs with magnetite suspensions stabilized at pH 3-10 were conducted. They proved that iron was released from magnetite at pH ≤ 6 through acidic dissolution (see XRD patterns and Mössbauer spectra in Figures S1 and S3). Moreover, the magnetite to maghemite conversion ratio obtained from Mössbauer spectrometry and from ICP-AES measurements were consistent[48] and proved that the acidic dissolution / oxidation[58-59] follows the reaction:

$$Fe_3O_4 + 2H^+ \rightarrow Fe_2O_3 + Fe^{2+} + H_2O \qquad (1)$$

The short stabilization time (overnight) at pH 5 may explain why Goberna-Ferron[26] did not observe $Fe(II)_{aq}$ in their solutions.

Magnetite diffraction peak widths were similar for solids stabilized at pH 4 and 8 (Figure S1), ruling out a significant change of magnetite crystal size in this pH range, in agreement with other studies.[58,60] The two low intensity peaks at 2.9 and 3.2 ^{0}, however, which are visible only in diffractograms measured at the synchrotron and not in the those measured with a laboratory source, as well as peaks shifting to higher values due to a shorter unit cell parameter, demonstrate a significant magnetite to maghemite transformation at pH 4 (62 %, Figure S1). As an example, the Mössbauer spectra recorded for the mineral stabilized at pH 3 (Figure S3), which contained >80 % of maghemite, showed sharper and less bifurcated peaks than magnetite in positions typical of maghemite. Indeed, the Mössbauer spectra show rather symmetrical hyperfine structures at 300 K and 77 K, as maghemite does not undergo the Verwey transition that is consistent with a large content of Fe^{3+} species.

This oxidation/conversion process driven by an adsorption reaction, which traps mobile electrons on the surface sites,[53] is correlated with cation migration/electron hopping through the lattice, creating cationic vacancies to keep the charge balance.[49] Mobility of electrons on the octahedral magnetite sub-lattice renews the surface Fe^{2+}, but slows down with time, due to the increase in thickness of the passivation layer.[59,60] Reaction (1) is known to be reversible in the absence of the oxidizing agent:[33,61] by increasing the pH, aqueous iron re-adsorbs by epitaxial growth on the surface, and results in 'spinel iron'.[60] No migration of iron ions towards the interior of the particle occurs, but electrons and presumably protons are injected into the particle from the adsorbed layer.[62]

To conclude this section, batch sorption experiments with the initial magnetite concentration 10 g/L at pH 7 start with pure material, in line with iron concentration < 0.01 mmol/L measured between 10 minutes and 5 months. 1.9 mmol/L of iron detected after 10 minutes of sorption experiment in *Se(VI)_pH5* solution corresponds to 4.4 % of the maghemite, if no Se(VI) was introduced. Estimation of the initial value at time zero will be given in the next paragraphs.

Such an elementary understanding of the magnetite/maghemite chemistry was needed before discussing the sorption/reduction experiments on magnetite, because maghemite does not show any reducing capacity towards selenate and selenite oxyanions,[63-64] and may perturb the electron exchange if covering the magnetite core surface. It should be highlighted here that the exact location of the oxidized layers (whether maghemite forms a shell around a magnetite core,[52,65] or it is delocalized due to possible electron hopping between Fe^{2+} and Fe^{3+} positions) is not within the scope of the present study.

Se(VI) sorption kinetics experiments on magnetite at pH 5 and 7

Results of the Se(VI) sorption experiments at pH 5 and 7 are given in Figure 1 and Table S1. Retention on magnetite was calculated from the ratio between the initial RN concentration (c_0) and the one measured by ICP-AES at a selected time interval (c_{aq}).

Se(VI) uptake was fastest during the first 10 days (240 h) in the two experimental series, while the rate depended on the solution pH, as reported in the literature.[28,66] At pH 7 during the first 10 days, 22 % of selenate was removed from the solution, while at pH 5 only 43 %. Thus, sorption was 1.9 times higher at pH 5 than that at pH 7 in the corresponding series (3.67 vs 1.86 mmol/L).

After the first 10 days, a plateau (within experimental error) was observed at pH 7 and the corresponding final selenate sorption extent was about 1.5 molecule/nm^2 of Se(VI). At pH 5 the removal process continued but at a much lower rate, reaching 53 % after 5 months, equivalent to about 4.2 molecule/nm^2 of Se(VI). It indicates that the theoretical sorption capacity (8 sites/nm^2) calculated for [Fe-OH] groups on the {111} crystallographic faces of magnetite[40] was only partially reached, with a level of 53 % at pH 5, and 22 % at pH 7, most probably due to the high concentrations of the adsorbates.[26,67]

ICP-AES results were confirmed by IC measurements, which can distinguish the two soluble forms (Se(IV) and Se(VI)). The reduced, soluble $(Se(IV)O_3^{2-}$ oxyanion remained below the detection limit at both pH values, suggesting that the reduction processes took place at the mineral surface and not in solution during the 5 months of the reaction. However, due to the necessary sample dilution (IC Se(VI) upper detection limit 10 ppm), low concentrations of selenite (for

sample dilution equal 50, Se(IV) lower detection limit 0.5 ppm would give 25 ppm!) might not have been detected.

If no reduction occurred, we could have assumed that the negatively charged oxyanions were exclusively adsorbed via electrostatic attraction to the positively charged surface sites of magnetite or maghemite, below their isoelectric points ($IEP_{magnetite}$ = 6.4-8, $IEP_{maghemite}$ = 5.5-7.5)[68], as found for selenate and selenite absorbed on positively charged $FeOH_2^+$ groups of maghemite.[63-64]

Fe(II) aqueous

At pH 7 the concentration of $Fe(II)_{aq}$ stayed below 0.01 mmol/L during 5 months, so we could assume that the magnetite was fairly pure at t_0 (as confirmed by Mössbauer spectrometry) and that any further mineral transformation was the consequence of redox reactions between the mineral and selenium species.

At pH 5, after 10 minutes of reaction, 1.87 mmol/L of iron was detected in the solution as a result of pH stabilization and acidic dissolution of magnetite, prior to selenate injection. While the re-adsorption of $Fe(II)_{aq}$ on magnetite is not favored at pH 5 due to the positively charged mineral surface,[33,35] the presence of $Fe(II)_{aq}$ may catalyze changes in the chemistry of Se(VI), forming ternary surface complex. During the following 5 months of sorption experiments run at pH 5, a linear co-removal dependency between Se(VI) and $Fe(II)_{aq}$ was detected (Figure 1b). The initial ratio nFe(II)$_{aq}$/nSe(VI)$_{aq}$ in the solution was 0.3:1 (*Se(VI)_pH5*) and the following re-adsorption ratio was 1:2, so lower than expected for complete Se(VI) reduction by $Fe(II)_{aq}$, pointing rather to the secondary mechanism. There was no $Fe(II)_{aq}$ left after 168 days of Se(VI) experiment, but

already after 3 months only 0.04 mmol/L of iron was still available in solution (red arrow in Figure 1a and 1b). In fact the Se(VI) concentration in solution was not decreasing anymore, due to $Fe(II)_{aq}$ depletion. Extrapolation of the co-removal results allowed the estimation of an initial aqueous iron concentration at t_0 equal to 2.4 mmol/L, corresponding to the 5.6 % of maghemite initially present (before selenate injection). This represents one monolayer of maghemite for the averaged 15 nm diameter spherical particles, so that electron exchange between the surface and the core of the magnetite should still be possible.

Several studies have shown that reduction of environmental contaminants is effectively catalyzed by $Fe(II)_{aq}$ adsorbed on magnetite,[34,70] montmorillonite,[20] goethite and lepidocrocite[61] and zero-valent iron.[69] Examination of the reduction of selenate by ZVI[69] and the removal of arsenic by non-stoichiometric magnetite[35] demonstrated the importance of the initial $Fe(II)_{aq}$ concentration on the extent of pollutant reduction. Moreover, $Fe(II)_{aq}$ alone did not show significant Se(VI) reduction.[69]

Eh – redox potential

The stability and reproducibility of redox potentials (Eh) measured in the filtered solutions were difficult to achieve due to low ionic strength of the solution, lack of reaction equilibrium (especially at the early stages of batch experiments) and possible reactions at the electrode surface.[71] Only negative values of Eh were measured during the first 3 months of the reactions, confirming overall reducing environmental conditions. At pH 7, redox potential fluctuated between -0.15 and 0.25 V (Figure S4) during the three months of the experiment. At pH 5, initial 10 days period with more reducing conditions (Eh between -0.15 and -0.33 V), where the drop in Se(VI) concentration was the fastest, was followed by milder period between 10 days and 3 months

(Eh between 0 and -0.15). The general trends fit well with different stability domains of the Pourbaix Eh-pH diagrams (Figure S4). The thermodynamically most stable form at both pH was Fe^{2+} for iron, in agreement with dissolution reaction. For selenium at pH 7 conditions were favorable for Se(0), while at pH 5 for both, Se(0) and Se(-II) in a form of either HSe^- or H_2Se.

Mineral transformation – Mössbauer and XRD

Magnetite to maghemite transformation was revealed by both Mössbauer spectrometry and X-ray diffraction (Figure S5). In the Rietveld refinement process only little freedom was given to the magnetite and maghemite unit cell parameters (a +/- 0.005 Å) to avoid erroneous phase identification. Analysis of the selected solid samples showed a large correlation between the two techniques (Table 2 and Figure 2) at pH 5, where a significant degree of transformation occurred, while at pH 7 XRD tends to underestimate the maghemite percentage in comparison to Mössbauer. A shift of the XRD peaks related to mineral transformation at pH 5 between 6 h and 168 days is clearly visible in Figure S5b, especially at the higher angles, while at pH 7 (Figure S5d) the corresponding higher angle peaks tend to be superimposed. This could indicate that at pH 7 the low maghemite fraction is not significantly disturbing the magnetite crystal lattice (randomly distributed Fe^{3+} cations), or that the thin oxidized layer at the mineral surface is amorphous, thus not contributing to the Bragg peaks and only to diffuse scattering.

Another important observation is the strong correlation between the degree of magnetite oxidation and the Se(VI) uptake, as highlighted in Figure 2. At pH 7, 18 % (Mössbauer) of maghemite formed during the first 6 hours, concomitantly with 1.27 mmol/L of Se(VI) removed from solution,

which corresponds to 1 % of mineral conversion for every 0.07 mmol/L uptake of Se(VI). Between 6 h and 95 days the conversion rate slowed down to 0.035 mmol/L of Se(VI) for each 1 % of mineral, probably due to partial oxidation of magnetite surface[72] which blocked the electron transfer.

A detailed analysis of the XRD patterns revealed a new peak corresponding to the (100) plane of trigonal gray Se(0)[73] at 2.9 ^{0} (λ = 0.1907 Å, Figure S5c), which increased concomitantly with the Se(VI) uptake and the mineral transformation (1 % of Se(0) after 5 months at pH 7). The redox process describing the Se(VI) reduction to Se(0) and magnetite oxidation, with an exchange of 6 electrons can be written as:

$$6Fe_3O_4 + Se(VI)O_4^{2-} + 2H^+ \rightarrow 9Fe_2O_3 + Se(0) + H_2O \quad (2)$$

Based on this model equation, with the initial magnetite concentration fixed at 10 g/L, 0.1 g of maghemite (1 %) should appear after reduction of 0.07 mM of selenate oxyanion by magnetite (details of calculation in SI). At the same time, consumption of protons should increase the pH of the solution, as observed in all batch experiments. This ideal stoichiometry was only observed in the initial phase of the Se(VI) experiment at pH 7. While selenate was still available in the solution (6.5-7 mmol/L) after few months of the reaction, the limiting factor, which slows down the adsorption, must have been the access to reducing magnetite sites.

Magnetite reacting at pH 5 with Se(VI) for 168 days resulted in about 3.4 % of Se(0) (XRD fitting), but the main redox reaction describing the process (2) is more complicated, because of the presence of $Fe(II)_{aq}$ leading to a secondary reaction. In the combined magnetite/$Fe(II)_{aq}$ system the electrons

migrate within the bulk and across the solid water interface.[33,73] The partially oxidized, positively charged magnetite surface can adsorb negatively charged selenate and selenite,[36,64] but the magnetite surface is also renewed via $Fe(II)_{aq}$.

The estimated initial maghemite fraction at pH 5, before Se(VI) injection, was equal to 5.6 %, and increased to 24 % after 6 h. At the same time 1.55 mmol/L of selenate was removed from the solutions. This corresponds to a selenate concentration drop of 0.084 mmol/L for each 1 % of oxidized mineral (after subtraction of the maghemite present initially in the solid), thus more than [Se(VI)] drop estimated from equation (2). In the following 95 days, the selenate removal rate dropped down to 0.07 mmol/L per 1 % of mineral transformation. If we compare the whole period of 95 days for the experiments at both pH, without subtraction of the initial maghemite due to acidic dissolution, the same Se(VI) removal – mineral oxidation ratio is found (0.068 mmol/L for 1 % of mineral oxidation). However the redox reaction at pH 5 is much faster than at pH 7, due to the additional reducing agent ($Fe(II)_{aq}$) and positively charged mineral surface, and continues until $Fe(II)_{aq}$ is depletion of.

Se(VI) reduction – XAS and STEM

The time evolution of selenium speciation on magnetite in *Se(VI)_pH5* and *Se(VI)_pH7* experiments was determined by K-edge XANES spectroscopy, using iterative target transformation factor analysis (ITFA). All spectra collected for selected solid samples from the two experimental series were successfully fitted with two components: trigonal Se(0) gray and outer-sphere aqueous Se(IV) (Table 3, Figures 3). EXAFS data (Figure S6) confirms the presence

of the gray elemental form (in contrast to amorphous Se(0) red), and show even more clearly than XANES the presence of an oxygen shell indicative of Se(IV). While these two oxidation states were also reported as reduction products of selenate by magnetite and green-rust,[25-26] numerous literature examples show that selenite can be immobilized by iron containing minerals in form of stronger inner-sphere (creation of covalent of ionic bonds) or/and weaker outer-sphere (electrostatic driven sorption) complexes, depending on the experimental conditions.[4,63-64,74-75]

Initial Se(VI) was not detected on the solids, so either all selenate was reduced by electrons from structural Fe(II) in magnetite (at pH 7), or from both structural and aqueous Fe(II) (at pH 5), or the weakly adsorbed Se(VI) was removed during filtration.[26]

Selenate at pH 7 was not strongly attracted to the mineral surface, even after hypothetical initial reduction to Se(IV), due to pH conditions close to mineral isoelectric point (neutral surface). XANES data fitting showed that in *Se(VI)_pH7* series the dominating species was gray Se(0) (Figures 3-4), with a small and constant contributions from Se(IV) (20 %) detected between 3 hours and 62 days, but not at 95 and 293 days. The large share of Se(0) indicates that the main immobilization mechanism at pH 7 followed the reductive precipitation described by equation (2), with simultaneous oxidation of magnetite to maghemite, as revealed by Mössbauer data analysis. The presence of the usually soluble Se(IV) species associated with the solid phase suggests that a small fraction of selenate was reduced only to selenite at the solid – liquid interface (Se(VI) not detected in solid, Se(IV) not detected in liquid), due to increasing maghemite layer thickness. ICP-AES showed no more Se(VI) uptake after 2 weeks of the experiment, so about 30 % of maghemite, (equivalent to 3 layers), hindered easy electron transfer. The Se(IV) stayed weakly adsorbed on

the oxidized surface during the first 2 months, but desorbed after this period (Figure 4). This secondary immobilization reaction requires an exchange of only two electrons and no proton consumption (no $Fe(II)_{aq}$ at pH 7):

$$2Fe_3O_4 + Se(VI)O_4^{2-} \rightarrow 3Fe_2O_3 + Se(IV)O_3^{2-} \quad (3)$$

The *Se(VI)_pH5* XANES data at 3 h showed only the strong white line of gray Se(0), as a result of the fast reduction on the magnetite surface (despite the presence of maghemite, due to the acidic dissolution), which was renewed by $Fe(II)_{aq}$ cations being continuously re-adsorbed. This can be related to a fast Se(VI) drop in solution measured with ICP-AES during the first two weeks (Figure 1). The selenite fraction appeared at 31 days (18 %) and stayed nearly constant until 293 days (15 %).

Based on these data, we can hypothesize that during the initial phase there is a non-perturbed electron exchange between magnetite and selenate, assisted by $Fe(II)_{aq}$ re-adsorption. As mineral oxidation is faster than iron re-adsorption, more and more maghemite layers cover the magnetite core. In this situation, the aqueous iron can only provide a limited number of electrons, which leads to a partial reduction of selenate to selenite.

A monotonic Se(IV) concentration increase reported for solid green rust[25] was attributed to two parallel reduction processes (selenate to selenite and selenate to elemental selenium). The adsorbed selenite could not have been reduced to Se(0), due to the depletion of Fe(II) sites in the vicinity of the adsorption sites. But in our case the aqueous iron renews the mineral redox activity. As the co-removal ratio shows a linear dependence between 10 minutes and 5 months, we assume that the

$Fe(II)_{aq}$ adsorption site changes as a function of the available reducing sites on the magnetite surface. In the initial phase, there are many accessible electrons in the system due to a limited fraction of maghemite. This favors the fast reduction of selenate to Se(0) on the mineral surface and proton consumption, which increases the pH (equation (2)). A small increase in pH causes re-adsorption of the aqueous iron, as in the absence of selenate.[33] So here the aqueous iron only renews the reducing surface of the mineral, but the re-adsorption is spread over time and takes several weeks.

In the second phase, iron re-adsorbs on a thicker maghemite layer (faster magnetite electron consumption than electron donation from $Fe(II)_{aq}$), and only partially renews the reducing capacity of the mineral (an easy electron exchange with the remaining magnetite core is blocked). So the reducing power allows only for the selenate to selenite reduction, with the partially reduced oxyanion being adsorbed to maghemite,[64] in the form of thermodynamically favored Fe-$Se(IV)O_3$ species.[76] This reaction theoretically consumes two iron cations per selenate anion:

$$2Fe^{2+} + SeO_4^{2-} + 2H^+ \rightarrow 2Fe^{3+} + SeO_3^{2-} + H_2O \qquad (4)$$

but the real redox process is more complicated due to the presence of the underlying mineral.

Selected solids from sorption experiments (*Se(VI)_pH7*: after 10 minutes and 95 days; *Se(VI)_pH5*: after 10 minutes, 6 days, 95 days and 168 days) were examined with TEM, to probe the shape and size of magnetite particles and the selenium reaction products.

Pure magnetite appeared as a collection of rather spherical 5-50 nm diameter particles, which tend to aggregate together, even after redistribution in the ultrasonic bath (Figure S2). The pH 5 and 7 Se(VI) samples collected at 10 minutes also showed only magnetite grains in TEM images - their composition was confirmed by X-ray energy-dispersive spectroscopy (XEDS, data not shown). As XANES data fitting showed a clear signal from Se(0) at 3 hours (at both pH), the reduction and crystallization of selenium must have occurred between 10 minutes and 3 hours.

Finally, the sample collected after 6 days of reaction in the Se(VI) experiment at pH 5 showed several Se nanowires as bright elongated areas in the STEM-HAADF image and STEM-XEDS map (Figure 3 a-b), similar to that observed for goethite/magnetite at pH 8.[25] The largest crystals reached no more than 1 μm × 100-200 nm.

All the remaining samples showed the development of Se(0) nanowires, which have grown along the [001] direction, while their thickness remained comparable to the ones observed at 6 days. The examples in Figure 3 c-d, g-h show magnetite reacted with Se(VI) at pH 5 after 168 days and pH 7 at 95 days. This preferential one-dimensional Se growth direction along the [001] axis is typical of laboratory Se(0) crystals.[77-78] Two diffraction patterns measured on the particle attached to the wire and at the wire (Figure 3 e-f) were successfully indexed with Se(0) trigonal phase $P3_121$.[78] Other forms of Se(IV) were not detected.

Although the evidence for the existence of Se(0) nanowires in STEM-HAADF images is clear, it may seem contradictory to XRD data, where only a small percentage of the gray form was detected. This can be explained by an uneven distribution of wires in the magnetite matrix. Scanning different regions of the TEM grids showed plenty of spots where selenium was not detectable at

all on the STEM-XEDS maps, located close to regions with selenium concentrated in the form of wires. Just like selenium deficient and contaminated areas in the natural environment.

CONCLUSIONS

Our studies confirmed the ability of magnetite to remove selenate from water and showed that the removal mechanism is both pH and $Fe(II)_{aq}$ presence dependent. The highest removal percentage over the longest time period was observed at pH 5 in presence of $Fe(II)_{aq}$: 53 % of the initial 8.6 mmol/L selenate was removed from solution after 5 months. The lowest sorption was associated with pH 7 and the absence of $Fe(II)_{aq}$: 22 % of the initial 8.6 mmol/L selenate was removed over the comparable period.

While long trigonal Se(0) nanorods were identified in the STEM-HAADF images of samples collected after ≥ 6 days of reaction in both experiments, XANES analysis revealed presence of the additional selenite species in samples where the maghemite surface layer blocked easy electron transfer. The proposed mechanism suggests a fast complete reduction of Se(VI) to Se(0) at the initial phase of the sorption experiments, related to rapid fall in aqueous selenate. The process continues at pH 7 until the reducing power of the mineral is spent (10 days – plateau in Se(VI) concentration). Meanwhile, at pH 5, the initially dissolved Fe(II) partially renews the reducing capacity of the material, but due to the limited speed of electron delivery, is unable to complete the selenate reduction, and as a result, the incompletely reduced selenite adsorbs on the maghemite surface. Selenate uptake continues slowly until the $Fe(II)_{aq}$ is completely removed.

Environmental relevance

Highly mobile selenate is a concern for the nuclear waste and coal mining industries. Because of weathering of selenium bearing rocks, such as shales and coal, or of corrosion of steel canisters, used for spent fuel geological storage, this highly toxic element can escape into the surrounding environment. However in anoxic environments, pore space and corrosion products often contain Fe(II), which can actively participate in selenate reductive immobilization. Our study shows that, in anoxic conditions typical for waste storage, even partially oxidized nanomagnetite particles (6 % of maghemite, 94 % of magnetite) are still capable of reducing the highly mobile selenium oxyanions to immobile, stable Se(0) form. Moreover, the aqueous Fe(II) leached from the mineral during stabilization at pH ≤ 6 boosts the reduction process, due to the renewed reducing power of the mineral surface. This opens a new way for the control of selenium level a variety of critical effluents.

AUTHOR CONTRIBUTIONS

The manuscript was written through contributions of all authors. All authors have given approval to the final version of the manuscript.

FUNDING SOURCES

The postdoctoral contract of AP and research grant were funded by the European Joint Program on Radioactive Waste Management (EURAD - European Union's Horizon 2020, grant agreement No 847593).

ACKNOWLEDGMENTS

We thank to BM20 and ID31 beamlines at the ESRF for providing in-house beamtime for XAS and XRD measurements. Funding from the FUTURE WP of the EURAD European project is acknowledged.

ABBREVIATIONS

ICP-AES - Inductively Coupled Plasma Atomic Emission Spectroscopy

IC – Ion Chromatography

STEM – Scanning Transmission Electron Microscopy

HAADF - High Angular Angle Dark Field

RN - radionuclide

SAED - Selected Area Electron Diffraction

XANES – X-ray Absorption Near-Edge Structure

EXAFS – Extended X-ray Absorption Fine Structure

FIGURES AND TABLES

Table 1. Experimental conditions for batch experiments

Batch name	Magnetite concentration [g/L]	pH	Initial total Se(VI) concentration [mM]	Initial Se(VI) concentration [mg/L]
Se(VI)_pH 5	10	5	8.6	679
Se(VI)_pH 7	10	7	8.6	679

* magnetite surface area from BET = 70 g/m^2

Table 2. Degree of magnetite to maghemite conversion from Mössbauer at 77 K and XRD pattern modeling and versus selenium uptake from ICP-AES.

Se series	Sample collection time	% of magnetite to maghemite conversion from XRD data fitting	% of magnetite to maghemite conversion from Mössbauer data		Drop in Se concentration with respect to c_0 [mmol/L] from ICP-AES	Solid e$^-$ release per gram of solid	Se(VI) to Se(0) e$^-$ consumed per gram of solid	Layers of maghemite on 15 nm spherical nanoparticle (based on 77 K Mossbauer data)
			300 K	77 K				
Se(VI)_pH5	6 h	25(1)	15-20	24	1.55	3.9-6.5E20	5.6E20	2.5
Se(VI)_pH5	6 days	44(1)			3.05	1.4E21	1.1E21	
Se(VI)_pH5	95 days		61-70	64	4.40	1.6-1.8E21	1.6E21	8.1

Se(VI)_pH5	168 days	70(1)			4.58	1.8E21	1.7E21	
Se(VI)_pH7	6 h	9(1)		18	1.27	2.3-4.7E20	4.6E20	1.8
Se(VI)_pH7	6 days	10(1)			1.59	2.6E20	5.7E20	
Se(VI)_pH7	95 days			31	1.71	8.1E20	6.2E20	3.3
Se(VI)_pH7	168 days	10(1)			1.63	2.6E20	5.9E20	

535

536 **Table 3**. Se speciation fractions calculated from the iterative target transformation of XANES data.

Se series	Sample collection time	Se (0) gray	Se(IV)	Sum
Se(VI)_pH5	3 h	1.00	0.00	1.00
Se(VI)_pH5	31 d	0.82	0.18	1.00
Se(VI)_pH5	62 d	0.83	0.18	1.01
Se(VI)_pH5	293 d	0.83	0.15	0.99
Se(VI)_pH7	3 h	0.82	0.19	1.01
Se(VI)_pH7	31 d	0.80	0.20	1.00
Se(VI)_pH7	62 d	0.82	0.20	1.01
Se(VI)_pH7	95 d	1.00	0.00	1.00
Se(VI)_pH7	293 d	1.00	0.01	1.00

537

538

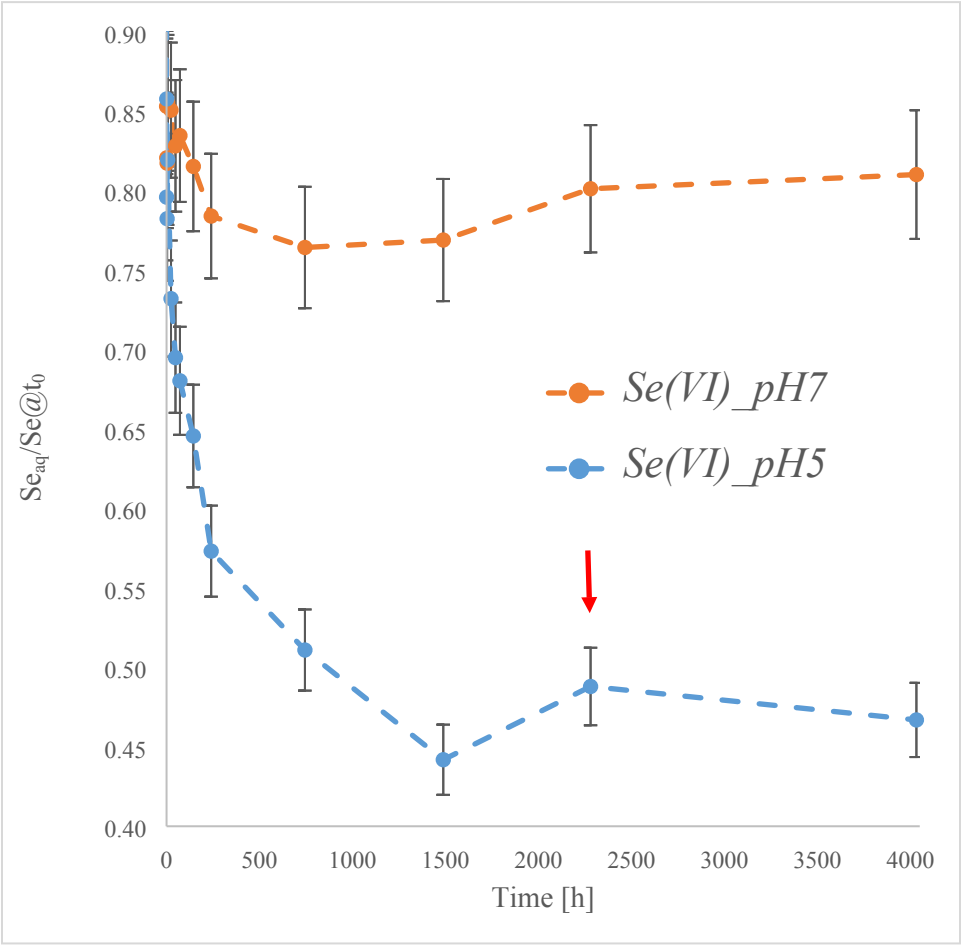
0.90
0.85
0.80
0.75
0.70
0.65
0.60
0.55
0.50
0.45
0.40
$Se_{aq}/Se@t_0$
0
500
1000
1500
2000
2500
3000
3500
4000
Time [h]
Se(VI)_pH7
Se(VI)_pH5

539

540

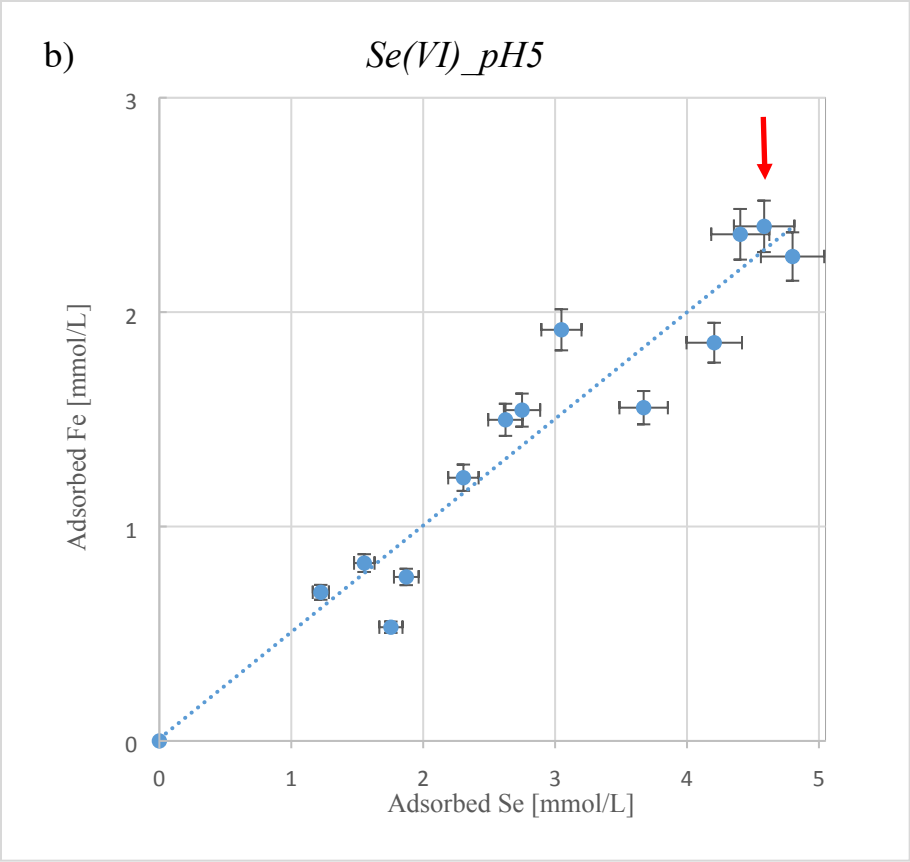

Figure 1. Sorption kinetics of RNs observed in the two batch experiments: a) Se(VI) and b) Linear dependence between Se(VI) and Fe(II) sorption found in the experiment at pH 5. As the Fe(II) first measurement was done at 10 min, concentration at time 0 was estimated by interpolation of the linear fitting. Red arrow indicate time of nearly complete adsorption of Fe(II) in *Se(VI)_pH5* experiment. Error bars represent 5 % error of the ICP-AES measurements.

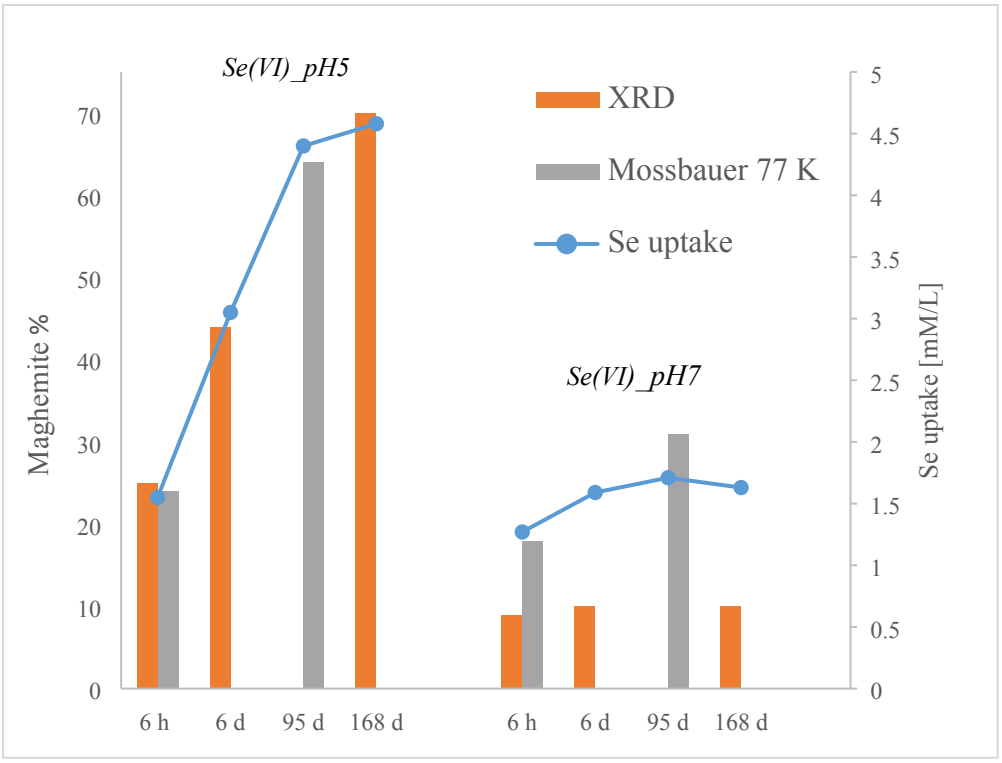

549

550 **Figure 2**. Degree of magnetite to maghemite conversion from Mössbauer at 77 K (gray bars) and

551 XRD pattern modeling (orange bars) *vs.* selenium uptake from ICP-AES (blue circles).

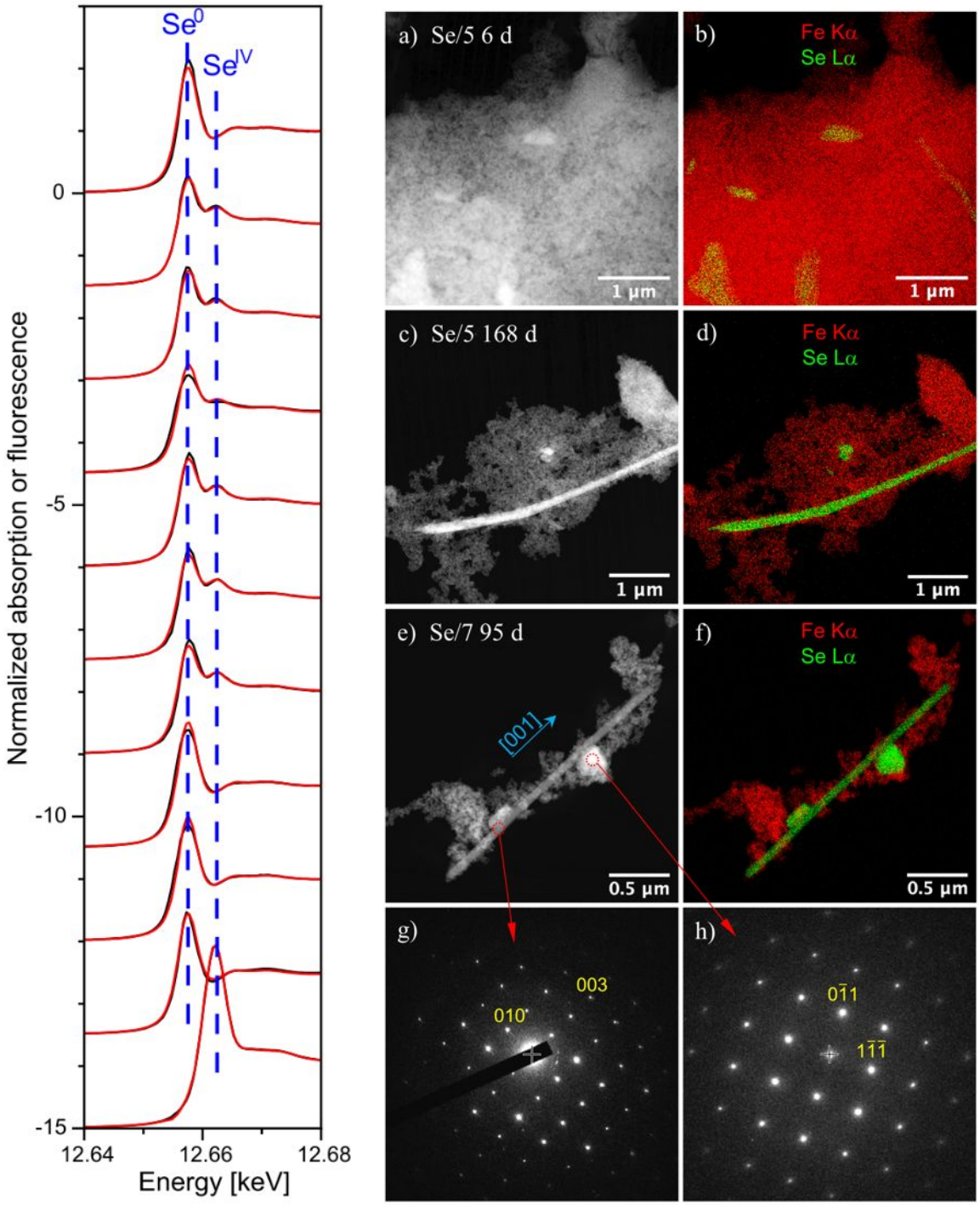

552

553 **Figure 3.** XANES: Selenium K-edge XAFS spectra of the two time series of Se(VI) experiments

554 at pH 5 and 7, and the two standard spectra (Se(0) gray and Se(IV) outer sphere). Black lines –

experimental data, red lines: reconstruction with two components. STEM-HAADF images (a, c, e) and STEM-XEDS maps (b, d, f) of magnetite-Se samples: a-b) *Se(VI)_pH5*, after 6 days – several selenium crystal seeds; c-d) *Se(VI)_pH5*, after 168 days -with 5 μm long selenium nanowire ; e-h) *Se(VI)_pH7*, after 95 days – 2.5 μm long nanowire with small selenium seeds; g) [100] zone axis of $P3_121$ Se(0); h) [211] zone axis of $P3_121$ Se(0).

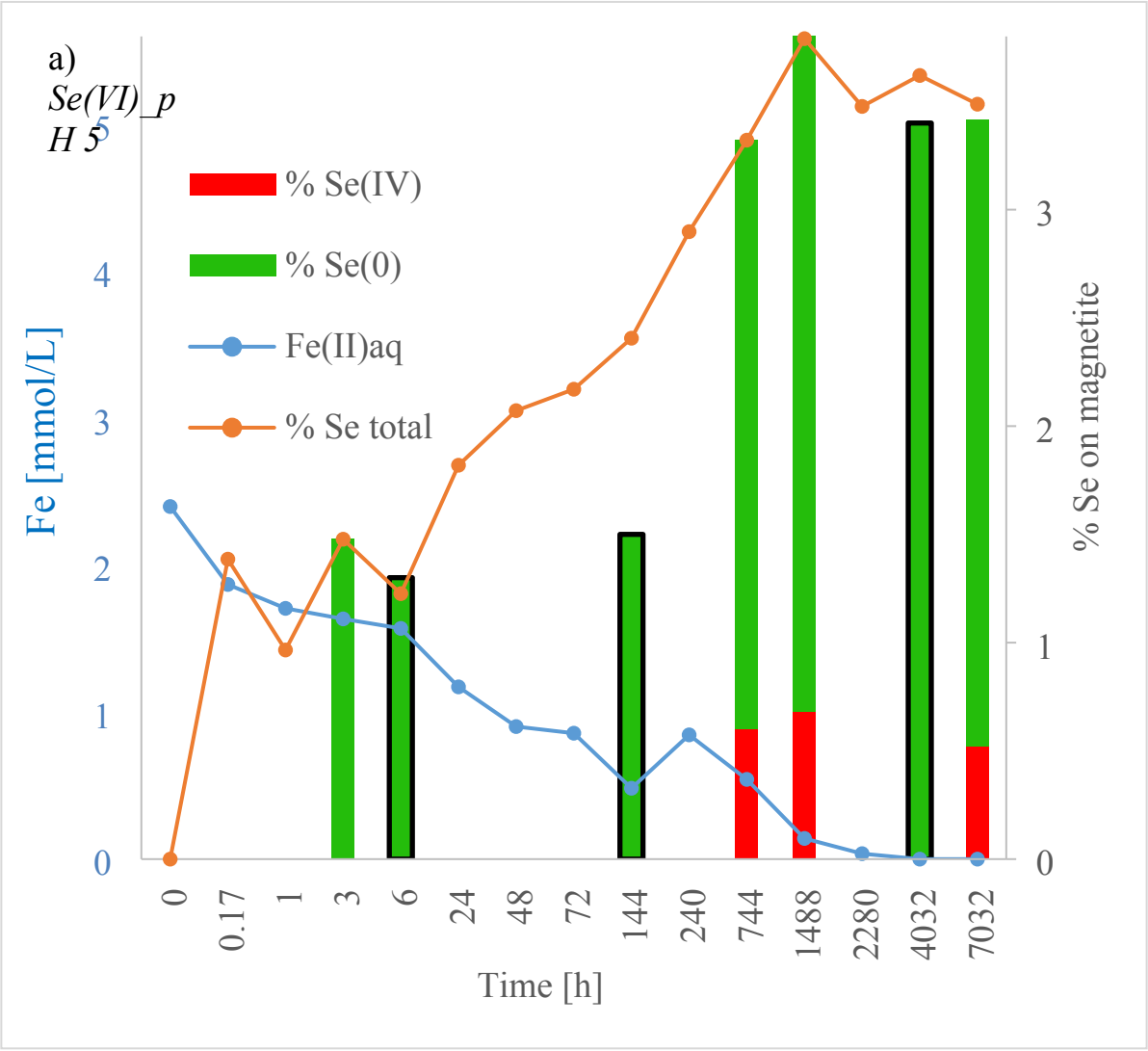

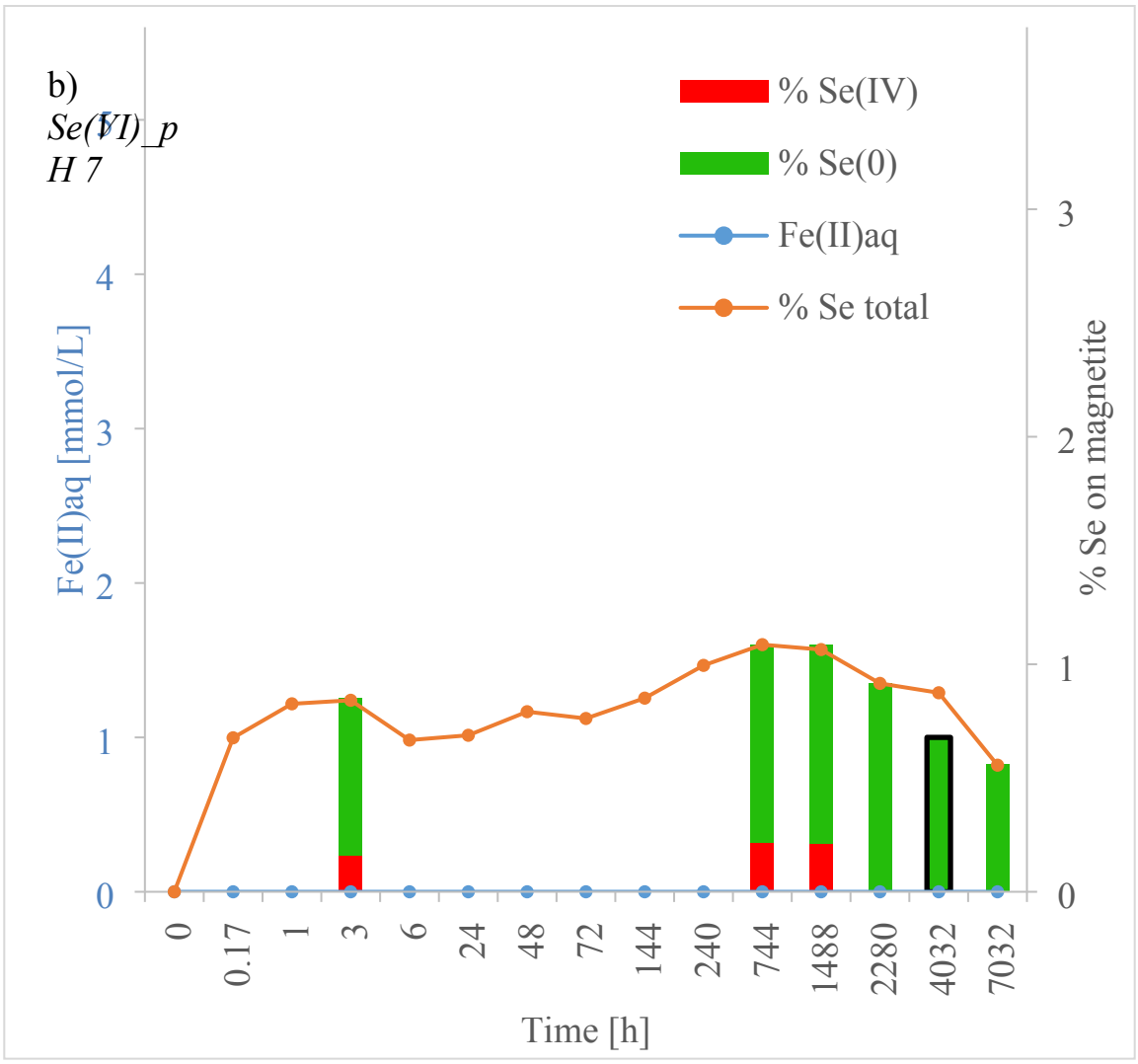

Figure 4. Summary of Fe(II)aq uptake (from ICP-AES: blue dots and line), Se(VI) uptake (from ICP-AES: orange dots and line), Se(0) fraction on magnetite (from ICP-AES/XANES – green bars – and XRD – green bars with black contours) and Se(IV) fraction (from ICP-AES/XANES: red bars) in the four experimental series.

REFERENCES

1. Levander, O.A., Burk, R.F. 2006. Update of human dietary standards for selenium. In: Hatfield, D.L., Berry, M.J., Gladyshev, V.N., editors. Selenium: Its Molecular Biology and Role in Human Health. 2nd edition. New York, NY: Springer Science and Business Media, 399-410.

2. Stolz J.F., Basu P., Santini J.M., Oremland R.S. (2006), Arsenic and selenium in microbial metabolism. Annu Rev Microbiol., 60:107-30. doi: 10.1146/annurev.micro.60.080805.142053. PMID: 16704340.

3. Gebreeyessus, G.D., Zewge, F. (2019), A review on environmental selenium issues, SN Applied Sciences, 1-55.

4. Fernández-Martínez, A. and L. Charlet, (2009). Selenium environmental cycling and bioavailability: A structural chemist point of view. Reviews in Environmental Science and Biotechnology 8, 81-110.

5. He., Y, Xiang, Y., Zhou, Y., Yang, Y., Zhang, J., Huang, H., Shang, C., Luo, L., Gao, J., Tang, L. (2018), Selenium contamination, consequences and remediation techniques in water and soils: A review, Environmental Research, 164, 288-301.

6. Fordyce F.M. (2013) Selenium Deficiency and Toxicity in the Environment. In: Selinus O. (eds) Essentials of Medical Geology. Springer, Dordrecht. https://doi-org.gaelnomade-1.grenet.fr/10.1007/978-94-007-4375-5_16.

7. Presser, T.S., Luoma, S.N. (2009), Modeling of Selenium for the San Diego Creek Watershed and Newport Bay, California: U.S. Geological Survey Open-File Report, 1114, p48.

8. Hibbs, B.J. & Lee, M.M. (2000). Sources of Selenium in the San Diego Creek Watershed, Orange County, California, Department of Geological Sciences, California State University, Los Angeles.

9. Meixner, T., Hibbs, B., Sjolin, J., Walker, J. (2004), Sources of Selenium, Arsenic and Nutrients in the Newport Bay Watershed, SWRCB- Agreement #00-200-180-01 Final Report of April 30th, 2004.

10. Shah, P., Strezov, V., Stevanov, C., Nelson, P.F., (2007), Speciation of Arsenic and Selenium in Coal Combustion Products, Energy & Fuels 21 (2), 506-512.

11. Okibe, N., Sueishi, K., Koga, M., Masaki, Y., Hirajima, T., Sasaki, K., Heguri, S., Asano, S. (2015), Selenium (Se) Removal from Copper Refinery Wastewater Using a Combination of Zero-Valent Iron (ZVI) and Se(VI)-Reducing Bacterium, Thaurea selenatis, Materials transaction 56(6), 889-894.

12. Khamkhash, A., Srivastava, V., Ghosh, T., Akdogan, G., Ganguli, R., Aggarwal, S. (2017), Mining-Related Selenium Contamination in Alaska, and the State of Current Knowledge, Minerals, 7, 46.

13. Wen, H., Carignan, J. (2007), Reviews on atmospheric selenium: emissions, speciation and fate, Atmospheric Environment 41, 7151-7165.

14. Scalet, B.M., Slade, S., Kasper, A., Van Marcke Lummen, G., Gitzhofer, K., Van Limpt, H. (2006) Selenium emission from glass melting furnaces: formation, sampling and analysis. Glass Technol 47A, 29–38.

15. Rossini, P., Matteucci, G., Guerzoni, S. (2010), Atmospheric fall-out of metals around the Murano glass-making district (Venice, Italy), Environ Sci Pollut Res, 17, 40-48.

16. Twidwell, L.G.; Mccloskey, J.; Joyce, H.; Dahlgren, E.; Hadden, A. Removal of Selenium Oxyanions from Mine Waters Utilizing Elemental Iron and Galvanically Coupled Metals. In Proceedings of the Jan D. Mill Symposium—Innovations in Natural Resource, Salt Lake City, UT, USA, 28 February–2 March 2005;pp. 299–313.

17. Etteieb, S., Magdouli, S., Zolfaghari, M., Brar, S. (2020), Monitoring and analysis of selenium as an emerging contaminant in mining industry: A critical review, Science of The Total Environment 698, 134339.

18. ANDRA (2005) Dossier 2005 Argile. Evaluation de sureté du stockage géologique. Agence National pour la gestion des Déchets Radioactifs, Paris.

19. Altmann, S. (2008), 'Geo'chemical research: a key building block for nuclear waste disposal safety cases, J. Contam. Hydrol., 102(3-4), 174-179.

20. Charlet, L., Scheinost, A.C., Tournassat, C., Greneche, J.M., Gehin, A., Fernandez-Martinez, A., Coudert, S., Tisserand, D., Brendle, J., (2007), Electron transfer at the mineral/water interface: Selenium reduction by ferrous iron sorbed on clay, Geochimica et Cosmochimica Acta, 71, 5731-5749.

21. Scheinost, A. C., Kirsch, R., Banerjee, D., Fernandez-Martinez, A., Zaenker, H., Funke, H., & Charlet, L. (2008). X-ray absorption and photoelectron spectroscopy investigation of selenite reduction by FeII-bearing minerals. Journal of Contaminant Hydrology, 102(3-4), 228–245.

22. Ma, B., Charlet, L., Fernandez-Martinez, A., Kang, M., Made, B. (2019). A review of the retention mechanisms of redox-sensitive radionuclides in multi-barrier systems, Applied Geochemistry, 100, 414-431.

23. Myneni, S.C.B., Tokunaga, T.K., Brown, G. (1997), Abiotic Selenium Redox Transformations in the Presence of Fe(II,III) Oxides, Science 278(5340), 1106-1109.

24. Scheidegger, A.M., Grolimund, D., Cui, D., Devoy, J., Spahiu, K., Wersin, P., Bonhoure, I., Janousch, M., 2003. Reduction of selenite on iron surfaces: a micro-spectroscopic study. J. Phys. IV 104, 417–420.

25. Onoguchi A, Granata G, Haraguchi D, Hayashi H, Tokoro C. (2019), Kinetics and mechanism of selenate and selenite removal in solution by green rust-sulfate. R. Soc.open sci.6: 182147.

26. Goberna-Ferron, S., Asta, M.P., Zareeipolgardani, B., Bureau, S., Findling, N., Simonelli, L., Greneche, J.M., Charlet, L & Fernández-Martínez, A. (2021), Influence of Silica

Coatings on Magnetite-Catalyzed Selenium Reduction, Environ. Sci. Technol., 55, 3021-3031.

27. Scheinost, A.C. and L. Charlet, (2008). Selenite reduction by mackinawite, magnetite and siderite: XAS characterization of nanosized redox products. Environmental Science and Technology 42, 1984-1989.

28. Martinez, M., Gimenez,J., de Pablo, J., Rovira, M. & Duro, L. (2006), Sorption of selenium(IV) and selenium(VI) onto magnetite, Applied Surace Science, 252, 10, 3767-3773.

29. Curti, E., Aimoz, L. & Kitamura, A. (2013), Selenium Uptake onto natural pyrite, J Radioanal Nucl Chem, 295, 1655-1665.

30. Breynaert, E., Scheinost, A.C., Dom, D., Rossberg, A., Vancluysen, J., Gobechiya, E., Kirschhock, C.E.A. and Maes, A. (2010), Reduction of Se(IV) in Boom Clay: XAS solid phase speciation. Environ. Sci. Technol. 44, 6649-6655. DOI: https://doi.org/10.1021/es100569e

31. Breynaert, E., Bruggeman, C. & Maes, A. (2008), XANES-EXAFS analysis of se solid-phase reaction products formed upon contacting Se(IV) with FeS2 and FeS, Environ Sci Technol, 42(10), 3595-601.

32. Das, S., Lindsay, M.B.J., Essilfie-Dughan, J. & Hendry, M.J. (2017), Dissolved Selenium(VI) Removal by Zero-Valent Iron under Oxic Conditions: Influence of Sulfate and Nitrate, *ACS Omega, 2* (4), 1513-1522.

33. Peng, H., Pearce, C.I., Huang, W., Zhu, Z., N'Diaye, A.T., Rosso, K.M. & Liu, J. (2018), Reversible Fe(II) uptake/release by magnetite nanoparticles, Environ. Sci.: Nano, 2018,5, 1545-1555.

34. Li, Y, Wei, G., Liang, X., Zhang, C., Zhu, J. & Arai, Y. (2020), Metal Substitution-Induced Reducing Capacity of Magnetite Coupled with Aqueous Fe(II), ACS Earth Space Chem. 4, 905-911.

35. Gubler, R. & ThomasArrigo, L.K. (2021), Ferrous iron enhances arsenic sorption and oxidation by non-stoichiometric magnetite and maghemite, Journal of Hazardous Materials, 402, 123425.

36. Jolivet, J.P., Belleville, P., Tronc, E. and Livage, J. (1992), Influence of Fe(II) on the formation of the spinel iron oxide in alkaline medium, Clay Clay Min., 40, 531-539.

37. Kieffer, J. & Karkoulis, D.: PyFAI, a versatile library for azimuthal regrouping. 11th International Conference on Synchrotron Radiation Instrumentation (SRI), Jul 2012, Lyon, France. 5 p., 10.1088/1742-6596/425/20/202012.

38. Rodríguez-Carvajal, J. (2001), Recent Developments of the Program FULLPROF, in Commission on Powder Diffraction IUCr. Newsletter 26, 12-19.

39. J. Teillet and F. Varret, unpublished MOSFIT program, Université Le Mans France.

40. Wechsler, B. A.; Lindsley, D. H.; Prewitt, C. T. (1984), Crystal structure and cation distribution in titanomagnetites (Fe_3-$xTixO_4$). Am. Mineral. 69, 754−770.

41. Scheinost, A.C., Claussner, J., Exner, J., Feig, M., Findeisen, S., Hennig, C., Kvashnina, K.O., Naudet, D., Prieur, D., Rossberg, A., Schmidt, M., Qiu, C., Colomp, P., Cohen, C., Dettona, E., Dyadkin, V. and Stumpf, T. (2021) ROBL-II at ESRF: A synchrotron toolbox for actinide research. J. Synchrotron Rad. 28, 333-349. DOI: https://doi.org/10.1107/S1600577520014265.

42. Webb, S.M. (2005) Sixpack: a graphical user interface for XAS analysis using IFEFFIT. Physica Scripta T115, 1011-1014.

43. Ressler, T. (1998) WinXAS: a program for X-ray absorption spectroscopy data analysis under MS-Windows. Journal of Synchrotron Radiation 5, 118-122.

44. Rossberg, A., Reich, T. and Bernhard, G. (2003) Complexation of uranium(VI) with protocatechuic acid - application of iterative transformation factor analysis to EXAFS spectroscopy. Anal. Bioanal. Chem. 376, 631-638.

45. Yalçıntaş, E., Scheinost, A.C., Gaona, X. and Altmaier, M. (2016) Systematic XAS study on the reduction and uptake of Tc by magnetite and mackinawite. Dalton Trans. 45, 17874-17885. DOI: https://doi.org/DOI: 10.1039/c6dt02872a

46. Wyckoff, R.W.G., Crystal Structures, 2nd ed.~Interscience, NewYork, 1964.

47. Grau-Crespo, R. Al-Baitai, A.Y. Saadoune, I. De Leeuw, N.H. (2010), Vacancy ordering and electronic structure of γ-Fe2O3 (maghemite): A theoretical investigation, *J. Phys.: Condens. Matter* 22, 255401.

48. Gorski, C.A., Scherer, M.M. (2010), Determination of nanoparticulate magnetite stoichiometry by Mössbauer spectroscopy, acidic dissolution, and powder X-ray diffraction: A critical review, *American Mineralogist*, 95, 7, 1017-1026.

49. Gallagher, K.J., Feitknecht, W., Mannweiler (1968), Mechanism of oxidation of magnetite to gamma Fe_2O_3, Nature, 217, 5234, 1118-1121, DOI 10.1038/2171118a0.

50. Kim, W., Suh, C.-Y., Cho, S.-W., Roh, K.-M., Kwon, H., Song, K. & Shon, I.-J. (2012), A new method for the identification and quantification of magnetite-maghemite mixture using conventional X-ray diffraction technique, Talanta, 94, 348-352.

51. Winsett, J., Moilanen, A., Paudel, K., Kamali, S., Ding, K., Cribb, W., Seifu, D., Neupane, S., Quantitative determination of magnetite and maghemite in iron oxide nanoparticles using Mössbauer spectroscopy, SN Applied Sciences (2019) 1:1636 | https://doi.org/10.1007/s42452-019-1699-2.

52. Salazar, J.S., Perez, L., De Abril, O., Phuoc, L.T., Ihiawakrim, D., Vazquez, M., Greneche, J.M., Begin-Colin, S., Pourroy, G. (2011), Magnetic iron oxide nanoparticles in 10-40 nm range: composition in terms of magnetite/maghemite ration and effect on the magnetic properties., Chemistry of materials, 23, 6, 1379-1386.

53. Belleville, P., Jolivet, J.P., Tronc, E., Livage, J. (1991), Crystallization of Ferric Hydroxide into Spinel by Adsorption on Colloidal Magnetite, Journal of Colloid and Interface Science, 150, 2, 453-460.

54. Doriguetto, A.C., Fernandes, N.G., Persiano, A.I.C., Filho, E.N., Greneche, J.M. & Fabris, J.D. (2003), Characterization of a natural magnetite, Physics and Chemistry of Minerals, 30. 249-255.

55. Berry, F.J., Skinner, S., Thomas, M.F. (1998), ^{57}Fe Mössbauer spectroscopic examination of a single crystal of Fe_3O_4. J. Phys.: Condensed Matter 10:215–220.

56. Daou, T.J., Begin-Colin, S., Grenèche, J.M., Thomas, F., Derory, A., Bernhardt, P., Legare, P., Pourroy, G. (2007) Phosphate adsorption properties of magnetite-based nanoparticles, Chem. Mater. 19, 4494–4505.

57. Grenèche, J.M. 2013 Mössbauer Spectroscopy: Tutorial Book ed Y Yoshida and G Langouche (Berlin: Springer) pp 187–241 and references therein.

58. Jolivet, J.P., Chanéac, C., Tronc, E. (2004), Iron oxide chemistry: From molecular clusters to extended solid networks, Chem. Commun., 481–487.

59. White, A.F., Peterson, M.L., Hochella, M.F.Jr., Electrochemistry and dissolution kinetics of magnetite and ilmenite, Geochimica et Cosmochimica Acta, 58, 8, 1859-1875.

60. Jolivet, J.P. & Tronc, E. (1988), Interfacial Electron Transfer in Colloidal Spinel Iron Oxide. Fe_3O_4-γ-Fe_2O_3 in aqueous medium, Journal of Colloid and Interface Science, 125(2), 688-701.

61. Tronc, E. & Jolivet, J.P. (1984), Exchange and Redox Reactions at the Interface of Spinel-Like Iron Oxide Colloids in Solution: Fe(II) Adsorption , Adsorption Sci. Techn. 1, 247.

62. Jolivet, J.P., Tronc, E. & Chanéac, C. (2006), Iron oxides: From molecular clusters to solid. A nice example of chemical versality, Comptes Rendus Géoscience, 338, 488–497.

63. Jordan, N., Ritter, A., Foerstendorf, H., Scheinost, A.C., Weiß, S., Heim, K., Grenzer, J., Mucklich, A., Reuther, H. (2013), Adsorption mechanism of selenium(VI) onto maghemite, Geochimica et Cosmochimica Acta 103, 63-75.

64. Jordan, N., Ritter, A., Scheinost, A., Weiss, S., Schild, D. & Hubner, R. (2013), Selenium(IV) uptake by Maghemite (γ-Fe_2O_3), Environ. Sci. Technol. 2014, 48, 3, 1665–1674.

65. Dehsari, H.S., Ksenofontov, V., Moller, A., Jakob, G., Asadi, K. (2018), Determining Magnetite/Maghemite Composition and Core-Shell Nanostructure from Magnetization Curve for Iron Oxide Nanoparticles, The Journal of Physical Chemistry C, 122, 49, 28292-28301.

66. Kim, S.S., Min, J.H., Lee, J.K., Baik, M.H., Choi, J.-W., Shin, H.S. (2012) Effects of pH and Anions on the Sorption of Selenium Ions onto Magnetite, J. Environ. Radioact, 104, 1-6.

67. Jamali-Behnam, F.; Najafpoor, A. A.; Davoudi, M.; Rohani-Bastami, T.; Alidadi, H.; Esmaily, H.; Dolatabadi, M. (2018) Adsorptive Removal of Arsenic from Aqueous Solutions Using Magnetite Nanoparticles and Silica-Coated Magnetite Nanoparticles. Environ. Prog. Sustain. Energy, 37, 951−960.

68. Kosmulski, M. (2016), Isoelectric points and points of zero charge of metal (hydr)oxides: 50 years after Parks' review, Advances in Colloid and Interface Science, 238, 1-61.

69. Yoon, I.-H., Bang, S., Kim, K.-W., Kim, M.G., Park, S.Y. & Choi, W.-K. (2016), Selenate removal by zero-valent iron in oxic conditions: the role of Fe(II) and selenate removal mechanism, Environ Sci Pollut Res, 23, 1081-1090.

70. Klausen, J.; Troeber, S. P.; Haderlein, S. B.; Schwarzenbach, R.P.(1995), Reduction of substituted nitrobenzenes by Fe(II) in aqueous mineral suspensions. Environ. Sci. Technol., 29, 2396−2404.

71. Altmeier, M., Goana, X., Fellhauer, D. and Buckau, G (2010) Intercomparison of redox determination methods on designed and near-natural aqueous systems. KIT Sci. Report 7572, p. 24.

72. Schwaminger, S.P., Bauer, D., Fraga-Garcia, P., Wagner, F.E. & Berensmeier. (2017), Oxidation of magnetite nanoparticles: impact on surface and crystal properties, Cryst. Eng. Comm., 19, 246-255.

73. Cherin, P. & Unger, P. (1967), The crystal structure of trigonal selenium, Inorg. Chem. 6, 8, 1589-1591.

74. Peng, H.; Pearce, C. I.; N'Diaye, A. T.; Zhu, Z.; Ni, J.; Rosso, K. M.; Liu, J.(2019), Redistribution of electron equivalents between magnetite and aqueous Fe^{2+} induced by a model quinone compound AQDS. Environ. Sci. Technol., 53, 1863−1873.

75. Ma., B, Fernández-Martínez, A., Wang, K., Made, B., Henocq, P., Tisserand, D., Bureau, S. Charlet, L. (2020), Selenite Sorption on Hydrated CEM-V/A Cement in the Presence of Steel Corrosion Products : Redox vs Nonredox Sorption, Environ. Sci. Technol., 54, 2344-2352.

76. Missana T., Alonso, U., Scheinost, A.C., Granizo, N. & Garcia-Gutierrez, M. (2009), Selenite retention by nanocrystalline magnetite: Role of adsorption, reduction and dissolution/co-precipitation processes, Geochimica et Cosmochimica Acta, 73, 20, 6205-6217.

77. Sinha, A.K., Sasmal, A.K., Mehetor, K.S., Pradhan, M., Pal, T. (2014), Evolution of amorphous selenium nanoballs in silicone oil and their solvent induced morphological transformation, Chem. Commun., 50, 15733.

78. Xiong, S., Xi, B., Wang, W., Wang, C., Fei, L., Hou, H., Qian, Y. (2006), The Fabrication and Characterization of Single-Crystalline Selenium Nanoneedles, Crystal Growth & Design, 6, 7, 1711-1716.

79. McCann, D.R., Cartz, L. (1972). Bond distances and chain angle of hexagonal selenium at high pressure, Journal of Applied Physics 43, 11, 4473-4477.

SUPLEMENTARY INFORMATION

Nanowire selenium formation upon reaction of selenate with magnetite

*Agnieszka Poulain[1], Alejandro Fernandez-Martinez[1], Jean-Marc Greneche[2], Damien Prieur[3], Andreas C. Scheinost[3], Nicolas Menguy[4], Sarah Bureau[1], Valérie Magnin[1], Nathaniel Findling[1], Jakub Drnec[5], Isaac Martens[5], Marta Mirolo[5], Laurent Charlet[1]**

[1] Univ. Grenoble Alpes, Univ. Savoie Mont Blanc, CNRS, IRD, IFSTTAR, ISTerre, 38000 Grenoble, France

[2] Institut des Molécules et Matériaux du Mans, CNRS UMR-6283, Le Mans Université, Le Mans, F-72085, France.

[3] The Rossendorf Beamline at ESRF, 71 avenue des Martyrs, 38043 Grenoble, France, and HZDR Institute of Resource Ecology, Bautzener Landstrasse 400, 01328 Dresden, Germany

[4] Sorbonne Université, Muséum National d'Histoire Naturelle, UMR CNRS 7590, IRD. Institut de Minéralogie, de Physique des Matériaux et de Cosmochimie (IMPMC), 4 Place Jussieu, 75005, Paris, France

[5] ID31 beamline at ESRF, 71 avenue des Martyrs, 38043 Grenoble, France

a)

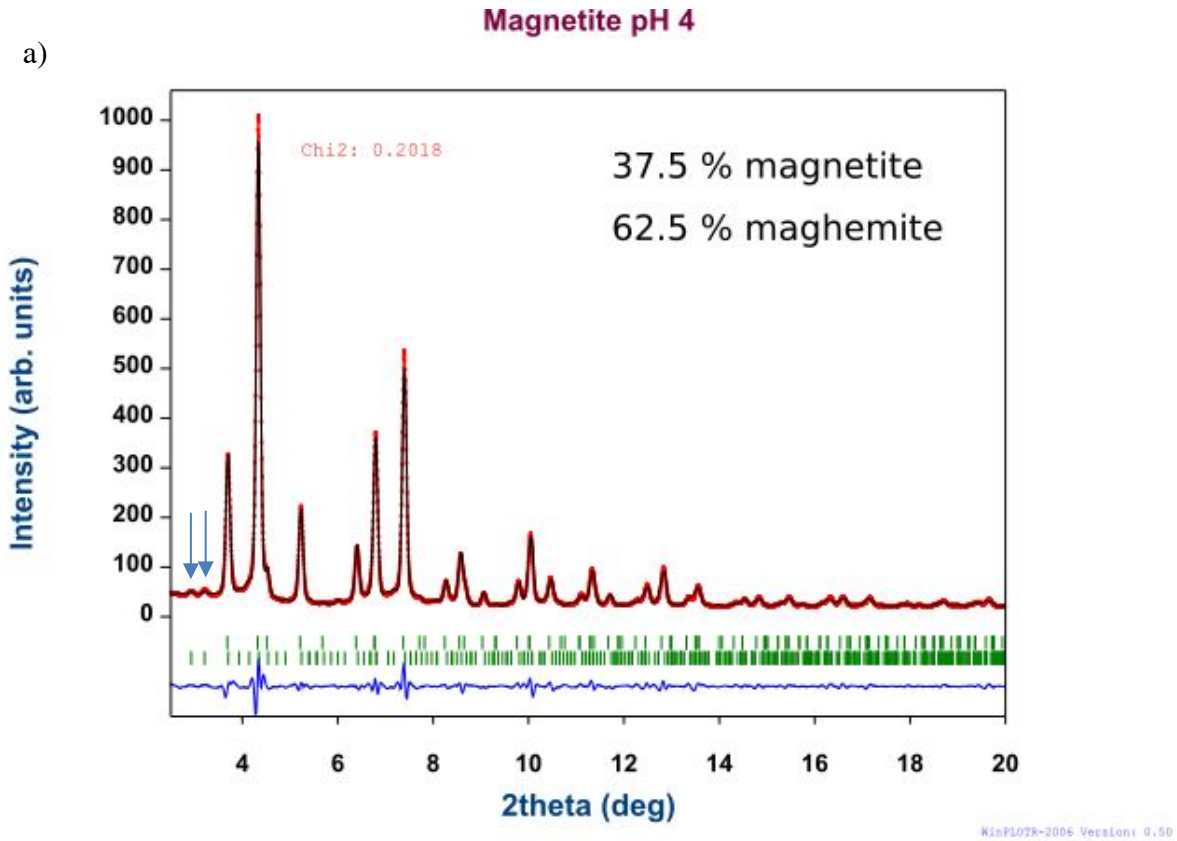
Magnetite pH 4
Chi2: 0.2018
37.5 % magnetite
62.5 % maghemite
Intensity (arb. units)
2theta (deg)
0
100
200
300
400
500
600
700
800
900
1000
4
6
8
10
12
14
16
18
20

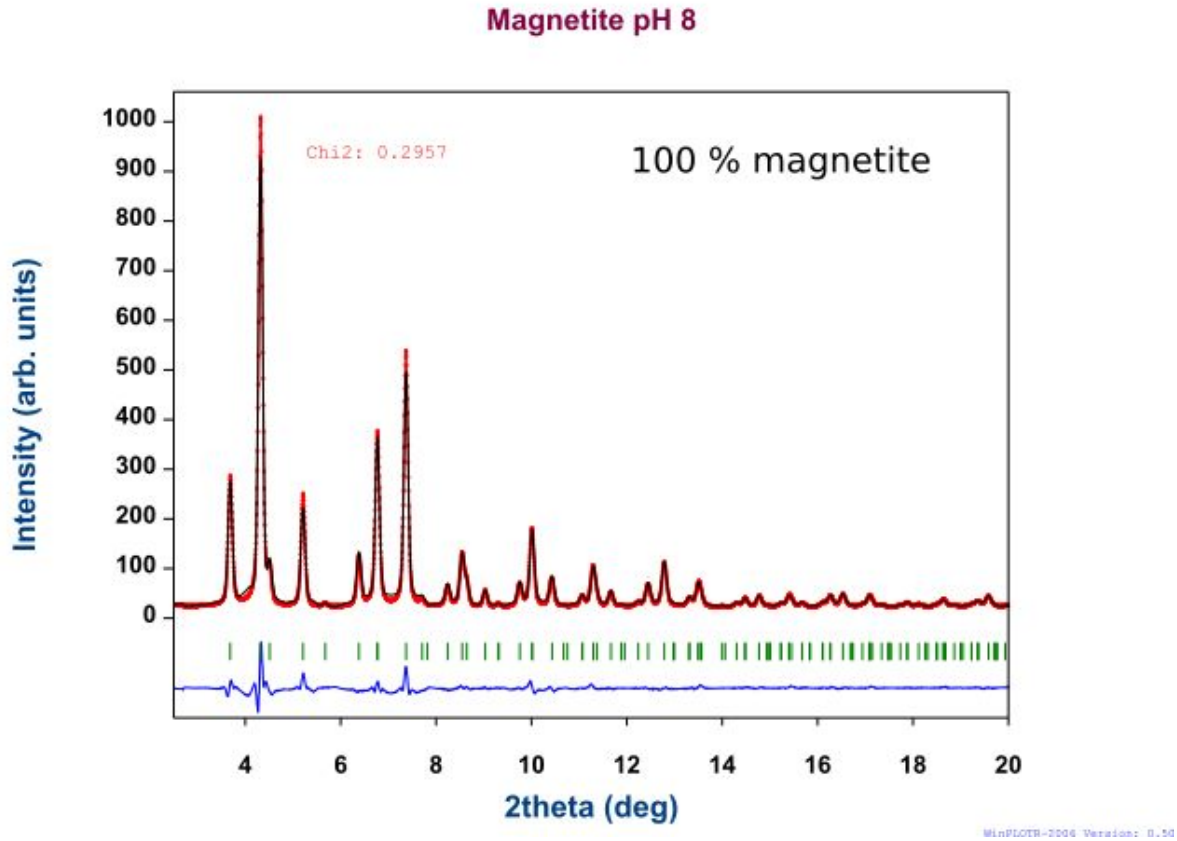
Magnetite pH 8
Chi2: 0.2957
100 % magnetite
Intensity (arb. units)
2theta (deg)
0
100
200
300
400
500
600
700
800
900
1000
4
6
8
10
12
14
16
18
20

819

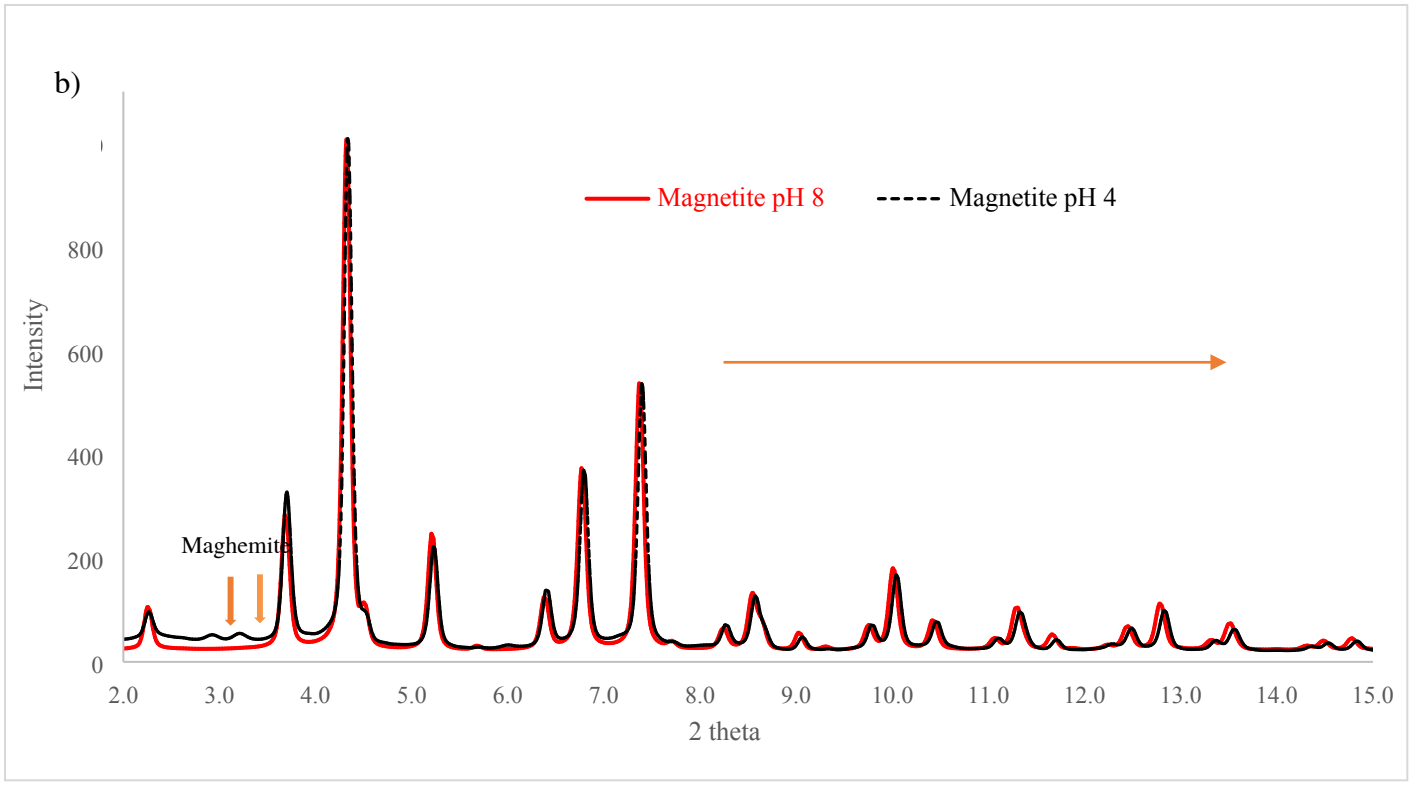
b)
Magnetite pH 8
Magnetite pH 4
Intensity
800
600
400
200
0
Maghemite
2.0
3.0
4.0
5.0
6.0
7.0
8.0
9.0
10.0
11.0
12.0
13.0
14.0
15.0
2 theta

820

821

c)

Figure S1. a) Fitting of XRD patterns of magnetite (a = 8.39 Å) stabilized at pH 4 and 8 (λ = 0.1907 Å). Imperfect fitting of the 3 most intense peaks come from memory effects of the detector. The two blue arrows show peaks of a similar intensity typical for maghemite (a = 3.42 Å). b) Superimposed patterns of Magnetite stabilized at pH 4 and 8 highlighting the peak shift due to magnetite transformation to maghemite and the new peaks at 2 theta = 2.9 and 3.2 ^{0}.

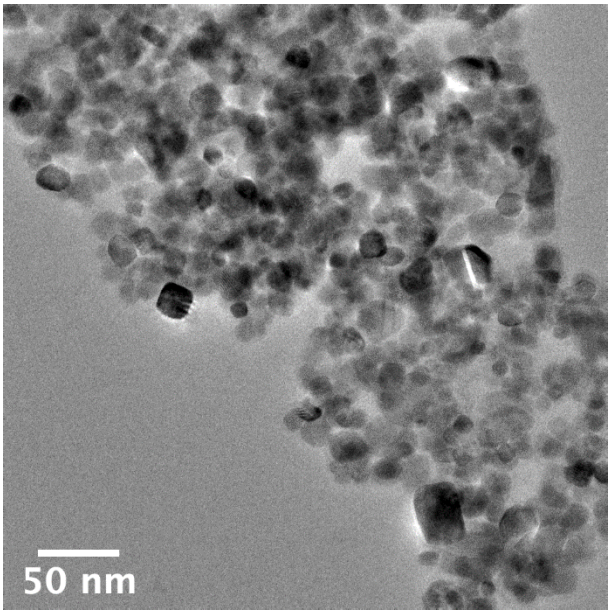

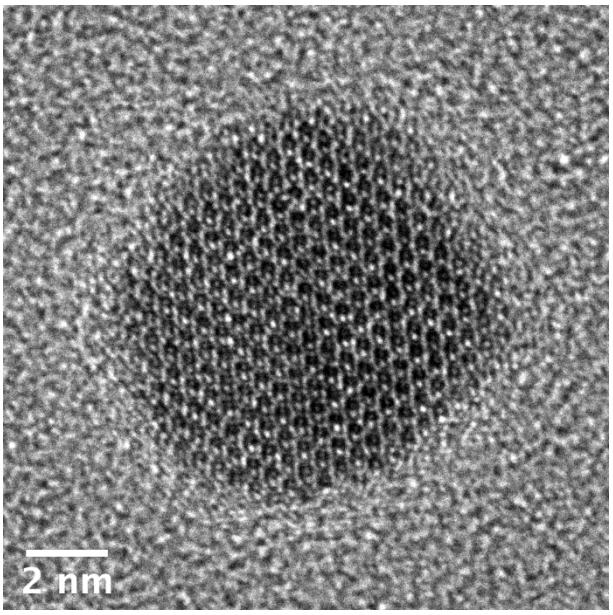

Figure S2. TEM images of the magnetite stabilized at pH 8: a) TEM – Bright Field, b) High Resolution TEM and corresponding FFT.

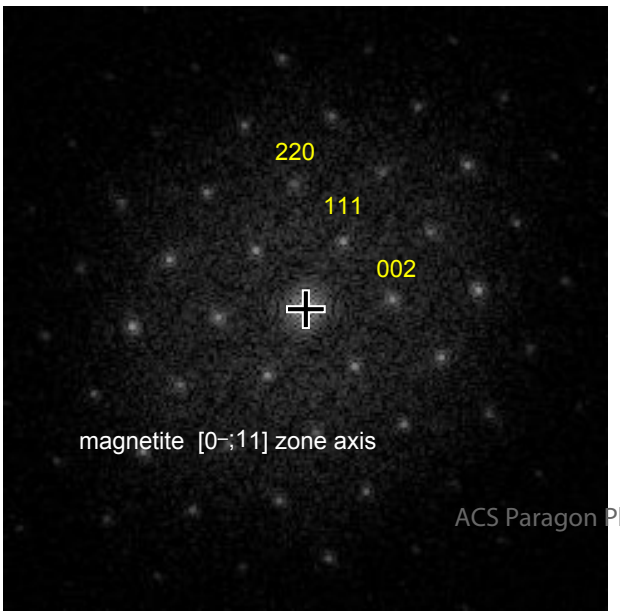

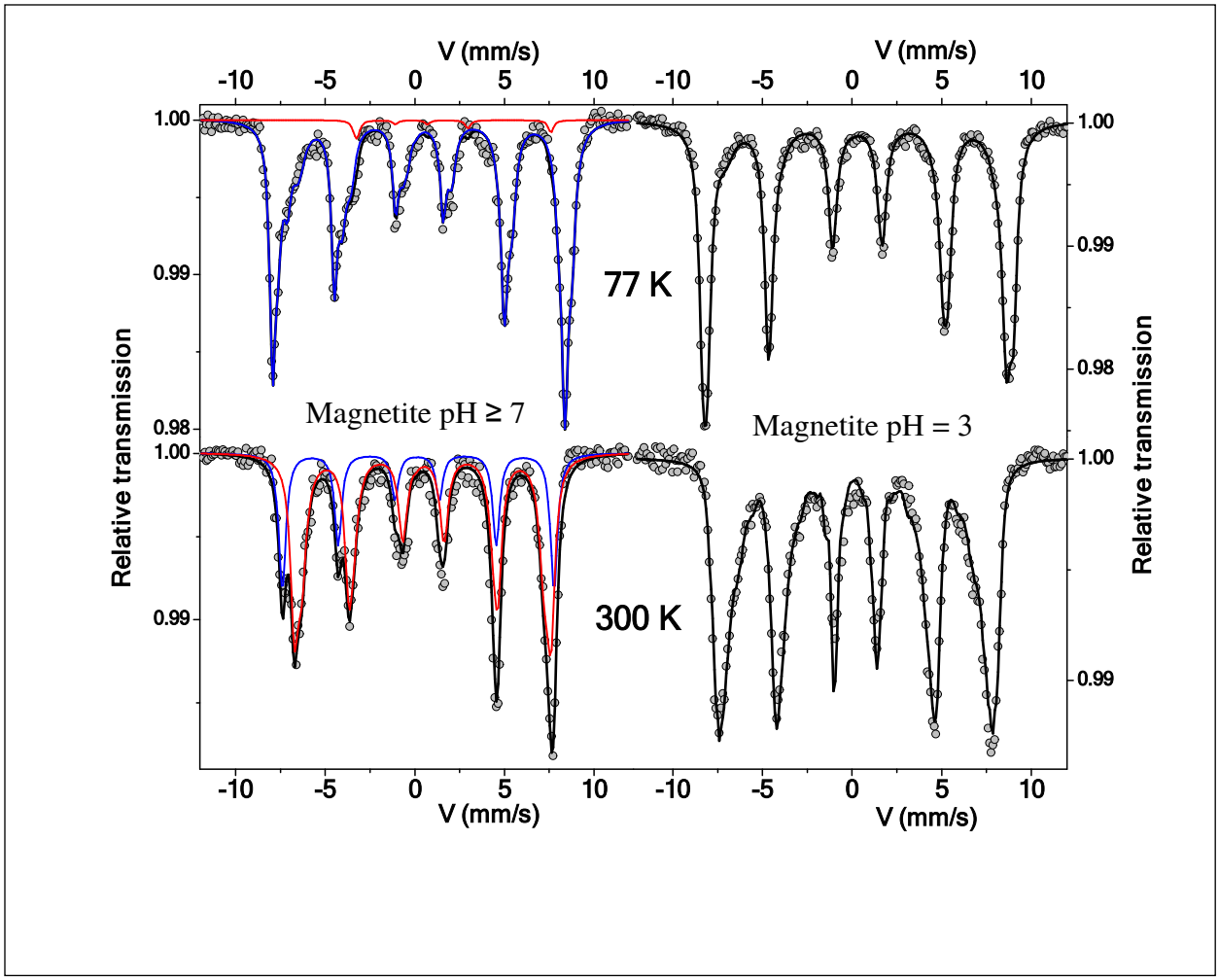

834 **Figure S3**. Left: Mössbauer spectra of the pure magnetite synthesized in a glovebox, measured at
835 77 K and 300 K, fitted with three components containing Fe(II) and Fe(III) species; Right:
836 Mössbauer spectra of the magnetite stabilized at pH 3, containing about 82 % of a maghemite at
837 77 K and 300 K.

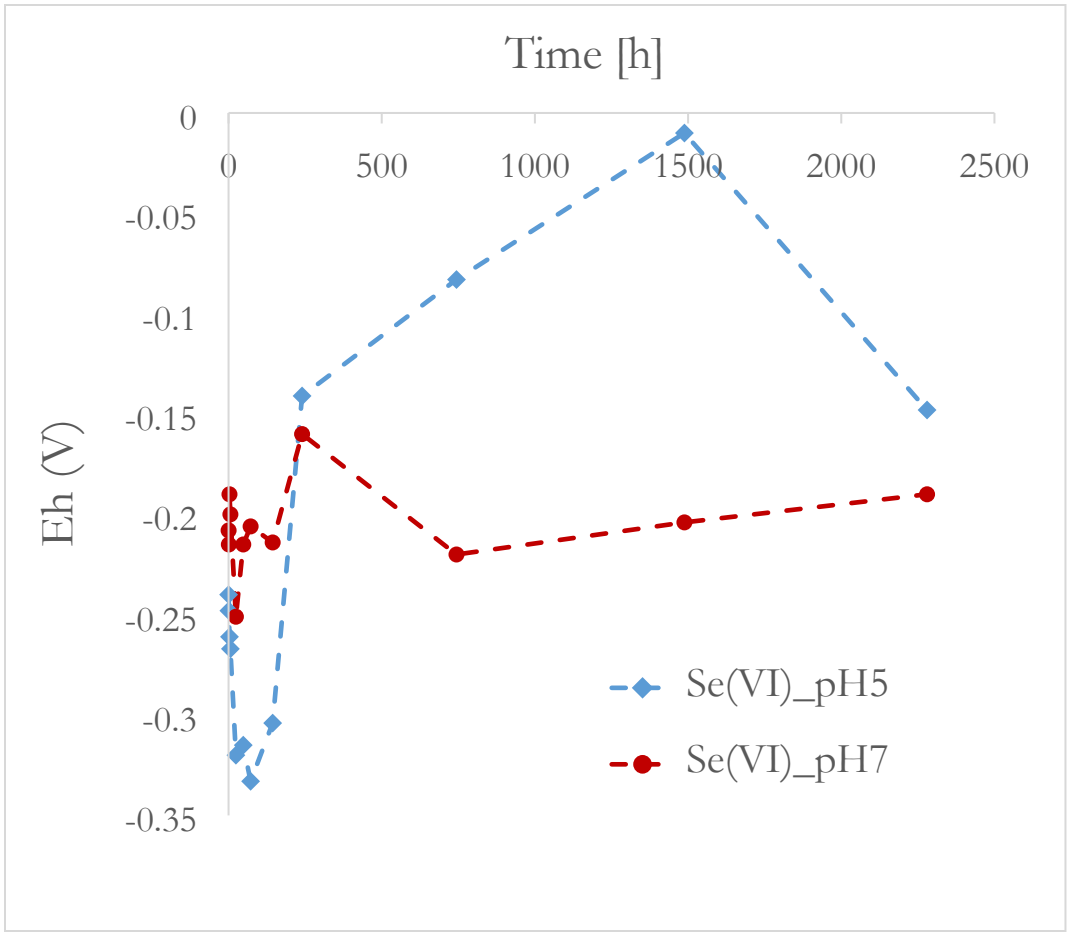
Time [h]
0
0
500
1000
1500
2000
2500
-0.05
-0.1
-0.15
-0.2
-0.25
-0.3
-0.35
Eh (V)
Se(VI)_pH5
Se(VI)_pH7

838

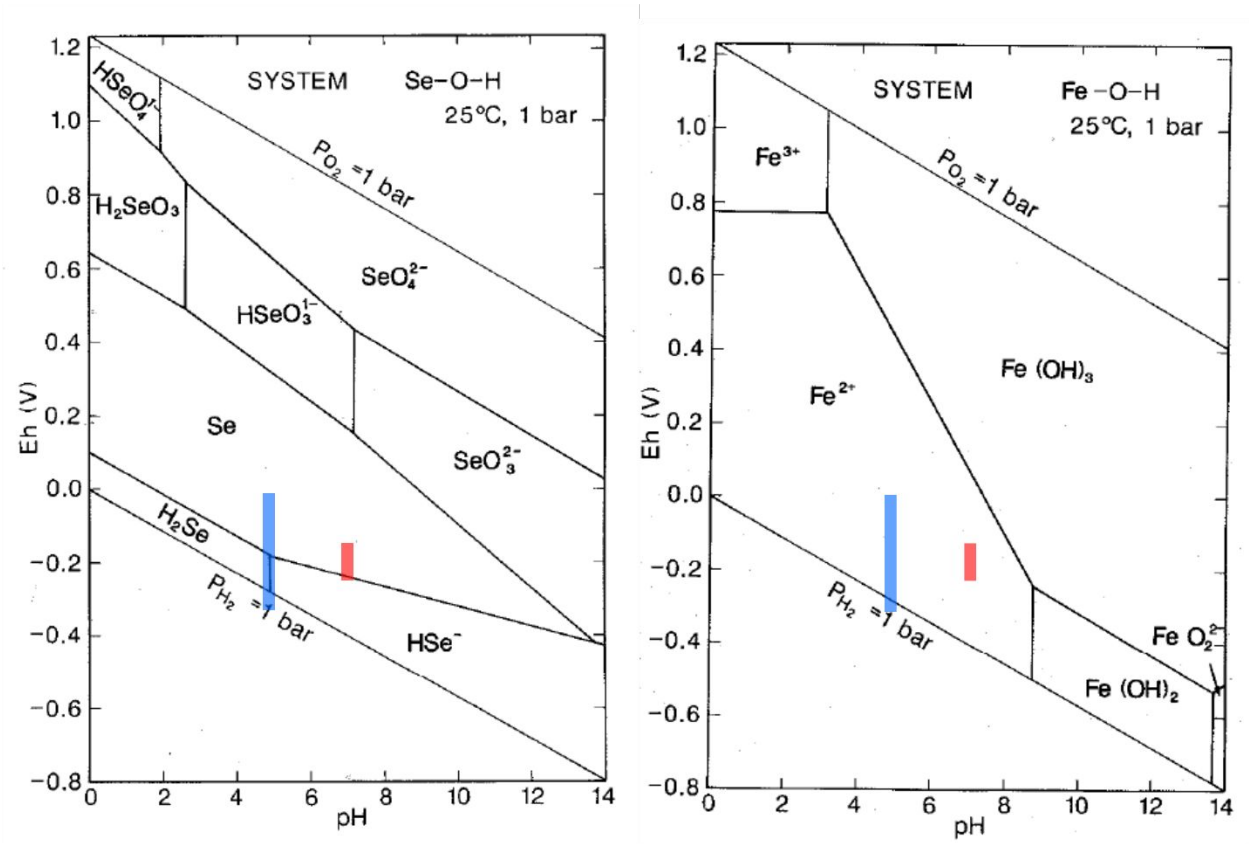

839

840 **Figure S4**. Fluctuation of redox potential during 3 months of sorption experiments and Pourbaix

841 diagrams (Brookins, D.G., (1988), Eh-ph Diagrams for Geochemistry, Springer) for Se and Fe,

842 showing redox potential – pH dependence of the thermodynamically stable phases. Blue:

843 Se(VI)_pH5 and red: Se(VI)_pH7.

844

845

a)

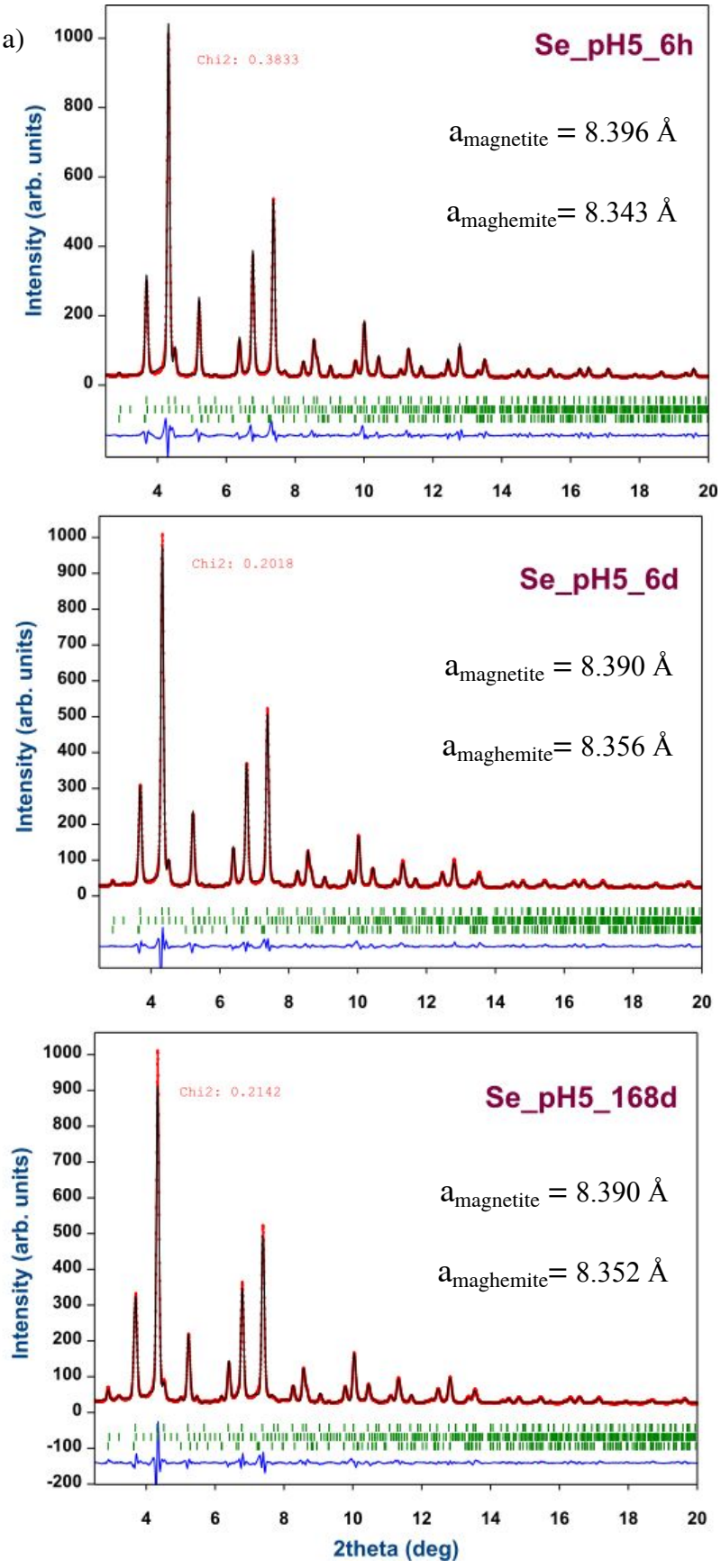
Chi2: 0.3833
Se_pH5_6h
$a_{magnetite}$ = 8.396 Å
$a_{maghemite}$= 8.343 Å
Chi2: 0.2018
Se_pH5_6d
$a_{magnetite}$ = 8.390 Å
$a_{maghemite}$= 8.356 Å
Chi2: 0.2142
Se_pH5_168d
$a_{magnetite}$ = 8.390 Å
$a_{maghemite}$= 8.352 Å
Intensity (arb. units)
2theta (deg)

846

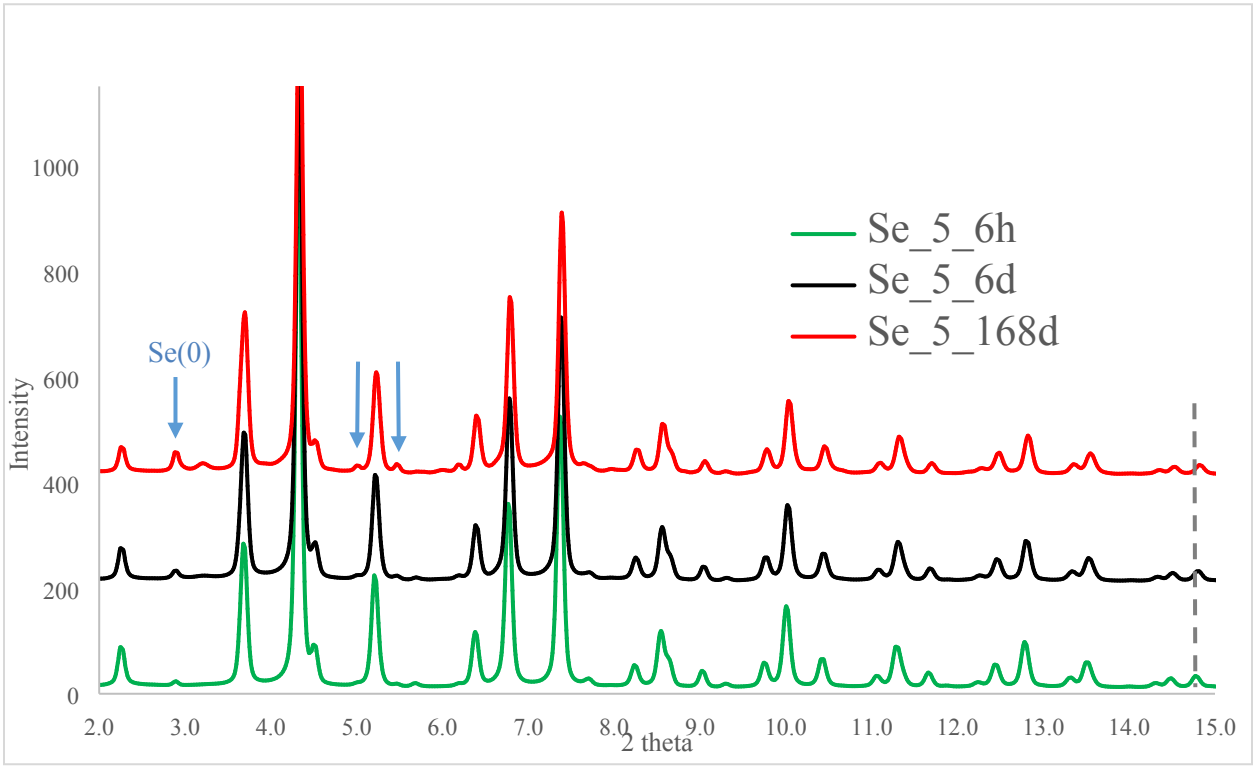
Se(0)
Se_5_6h
Se_5_6d
Se_5_168d
Intensity
2 theta
0
200
400
600
800
1000
2.0
3.0
4.0
5.0
6.0
7.0
8.0
9.0
10.0
11.0
12.0
13.0
14.0
15.0

c)

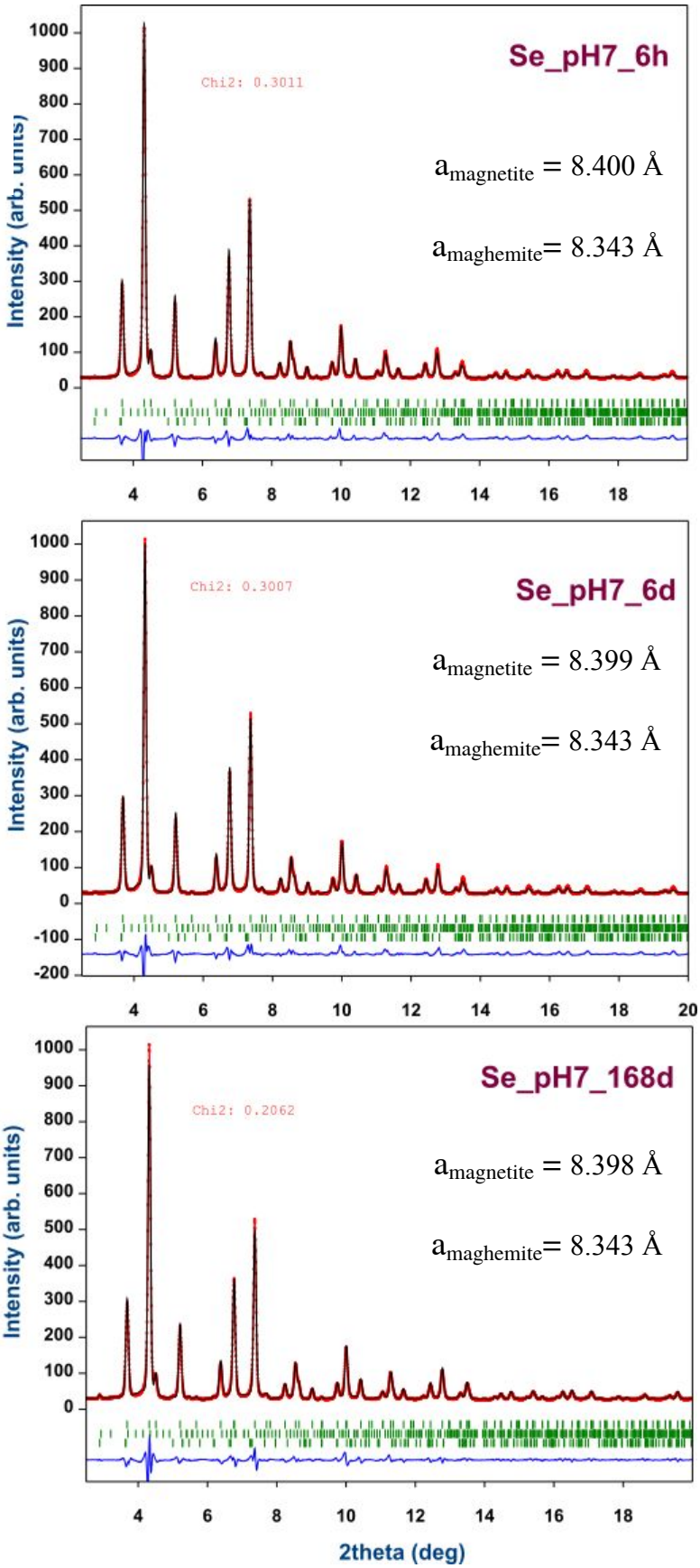
Se_pH7_6h
Chi2: 0.3011
$a_{magnetite}$ = 8.400 Å
$a_{maghemite}$= 8.343 Å
Se_pH7_6d
Chi2: 0.3007
$a_{magnetite}$ = 8.399 Å
$a_{maghemite}$= 8.343 Å
Se_pH7_168d
Chi2: 0.2062
$a_{magnetite}$ = 8.398 Å
$a_{maghemite}$= 8.343 Å
Intensity (arb. units)
2theta (deg)

850

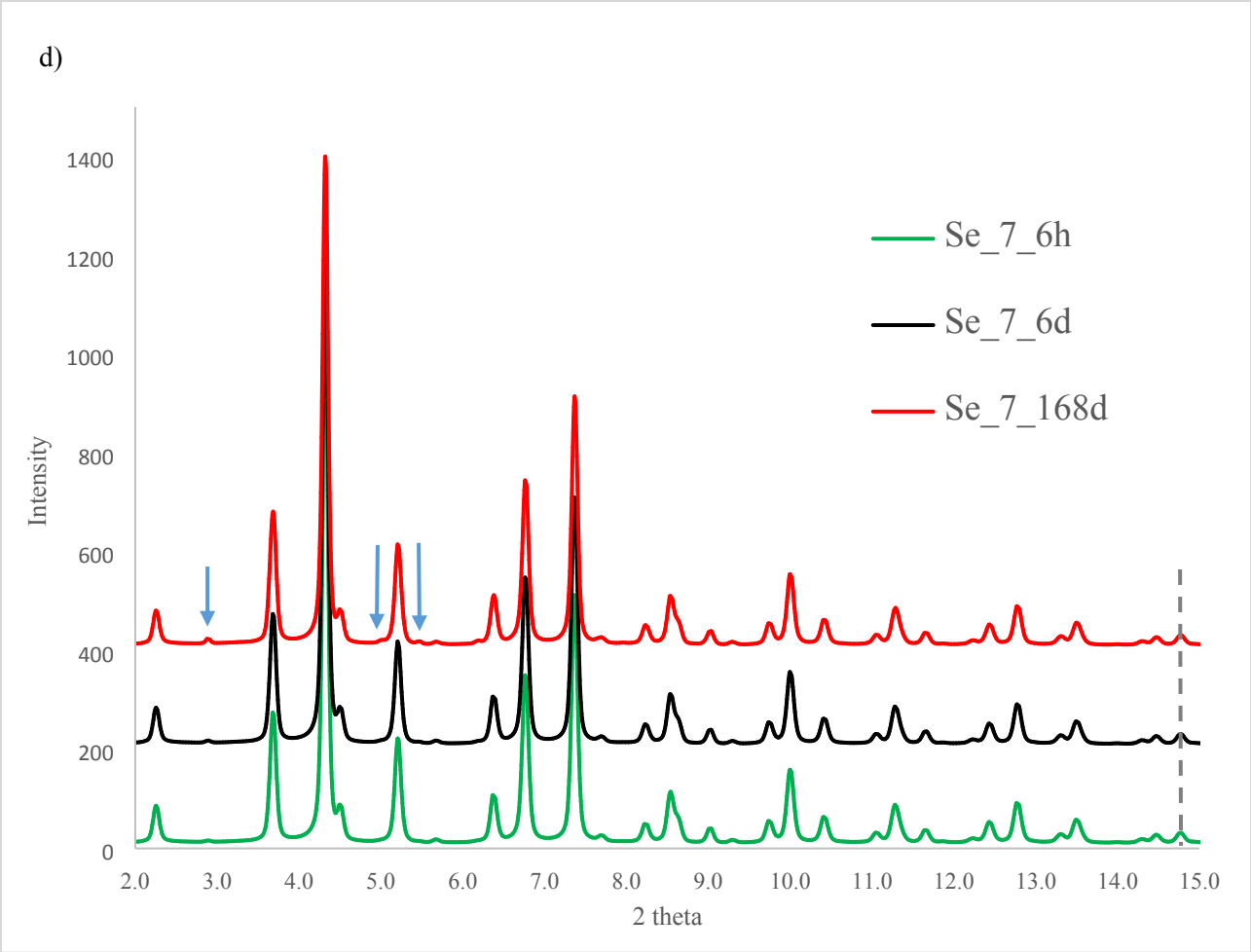

Figure S5. a) Results of Se(VI) sorption on magnetite at pH 5 (6 h, 6 days and 168 days) XRD Rietveld refinement with magnetite, maghemite and Se(0) trigonal; b) superimposed raw data for Se(VI) sorption on magnetite at pH 5. Blue arrows show peaks from Se(0); c) results of Se(VI) sorption on magnetite at pH 7 (6 h, 6 days and 168 days) XRD Rietveld refinement with magnetite, maghemite and Se(0) trigonal; d) superimposed raw data for Se(VI) sorption on magnetite at pH 7. Blue arrows show peaks from Se(0) – lower intensity than in pH 5 series; chi2 reflecting fitting quality is indicated in the figures. λ = 0.1907 Å.

Data at pH 5 show the shift of all peaks reflecting transformation to maghemite, while at pH 7 such a shift is not observed.

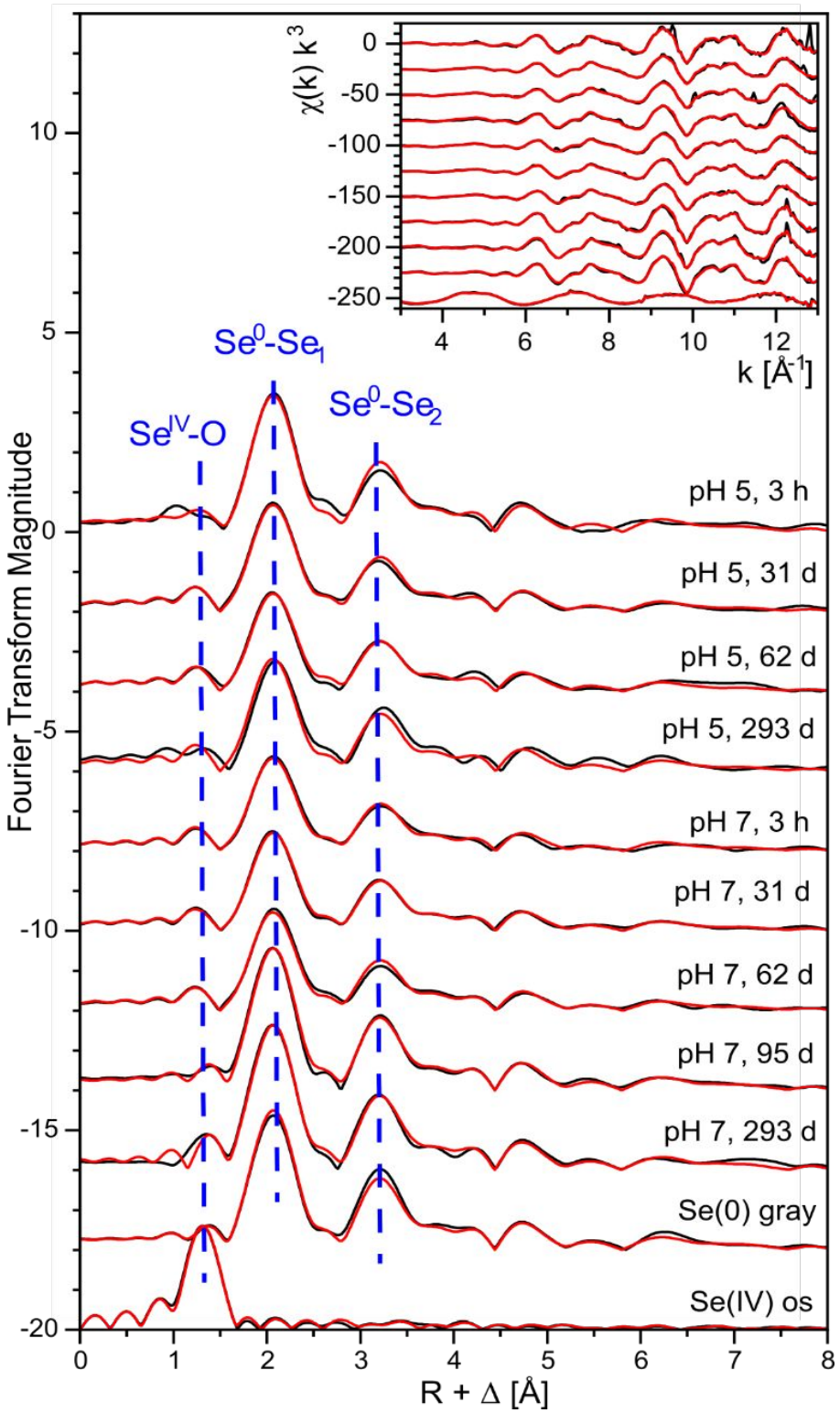
Fourier Transform Magnitude
R + Δ [Å]
χ(k) k³
k [Å⁻¹]
Se⁰-Se₁
Se⁰-Se₂
Seᴵⱽ-O
pH 5, 3 h
pH 5, 31 d
pH 5, 62 d
pH 5, 293 d
pH 7, 3 h
pH 7, 31 d
pH 7, 62 d
pH 7, 95 d
pH 7, 293 d
Se(0) gray
Se(IV) os

861

Figure S6. Selenium K-edge EXAFS spectra of selected Se(VI) magnetite samples, along with gray Se(0) and Se(IV) aquo references. Black lines: experimental data, red lines: reconstruction with two components.

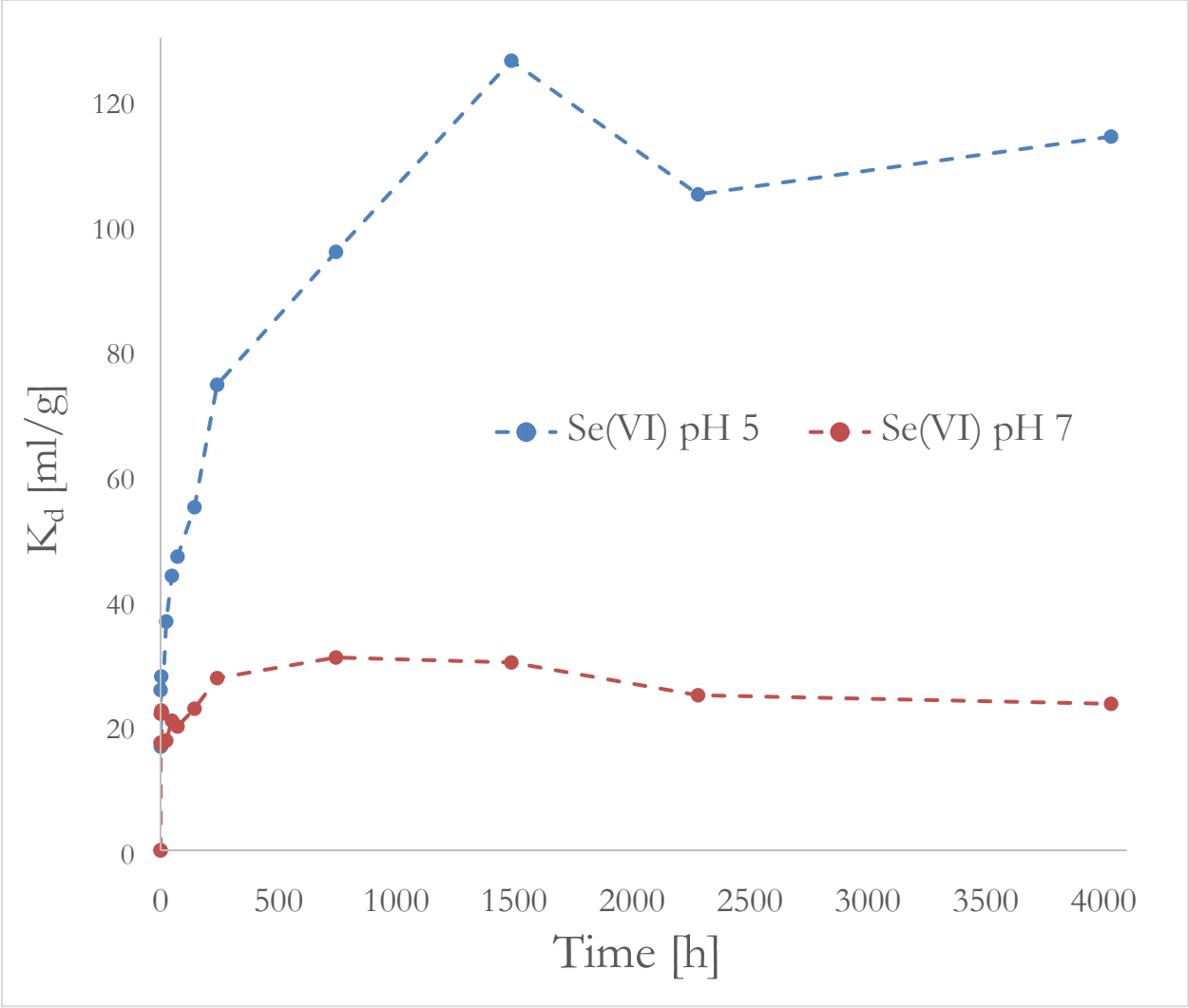

Figure 7. K_d value calculated for Se(VI) series at pH 5 and 7, reflecting Se partitioning between solid and liquid.

Table S1. Results of the kinetics sorption experiments. Magnetite concentration fixed at 10 g/L.

	Se(VI) pH 5		Se(VI) pH7	
Time [h]	Se in solution [ppm/L]	Fe in solution [ppm/L]	Se in solution [ppm/L]	Fe in solution [ppm/L]
0	679	144 (estimated)	679	
0.17	540.5	104.4	579.3	0.2
1	582.4	95.3	557.3	0.1
3	531.2	91.3	555.0	0.3
6	556.4	87.7	580.8	0.3
24	497.1	65.5	577.6	0.0
48	471.9	50.4	562.4	0.1
72	462.0	47.9	566.8	0.1
144	438.4	26.9	553.6	0.0
240	389.2	47.2	532.4	0.1
744	346.9	30.3	518.9	0.0
1488	300.0	7.9	522.1	0.0
2280	331.3	2.1	544.0	0.4
4032	317.0	0.0	550.1	0.4

Calculation based on magnetite to maghemite conversion oxidation and Se(VI) to Se(0) reduction.

Taking the initial magnetite concentration 10 g/L, one can calculate how much of selenium can be reduced for each 1 % of the mineral, if the redox reaction follows:

$$6Fe_3O_4 + Se(VI)O_4^{2-} + 2H^+ \rightarrow 9Fe_2O_3 + Se(0) + H_2O$$

Molar weights of the two minerals are:

Mw(magnetite) = 231.5 g/mol and Mw(maghemite) = 159.7 g/mol

1 % of the initial mineral (10g/L) gives 0.1 g. Due to difference in mineral mass on the left and right side (6 * Mw magnetite = 1389 g and 9 * Mw maghemite = 1437 g) we can consider 2 cases: i) how much Se(VI) is reduced for 0.1 g of magnetite, ii) how much Se(VI) is reduced for 0.1 g of maghemite.

From a simple proportion, we can calculate:

i) how much Se(VI) reacts with 0.1 g of magnetite, if 1389 g reacts with 1 mol of Se(VI)?

x = 0.1 g * 1 mol / 1389 g = 0.00072 mol = 0.072 mmol

ii) how much Se(VI) is needed to produce 0.1 g of maghemite, if 1437 g is produced using 1 mol of Se(VI)?

x = 0.1 g * 1 mol / 1437 g = 0.0000695 mol = 0.0695 mmol

Both results are close to **0.07 mmol**.

Calculations of the number of electrons per gram of solid released during magnetite oxidation and selenate reduction, if the reaction follows equation 3

$$6Fe_3O_4 + Se(VI)O_4^{2-} + 2H^+ + 6e^- \rightarrow 9Fe_2O_3 + Se(0) + H_2O + 6e^-$$

1) For 100 % mineral transformation in the above reaction 6 moles of magnetite need 6 moles of electrons. To calculate how many electrons per gram of solid is needed, we need Mw of magnetite (231.5 g/mol).

x = 1g * 6 * 6.02E23 electrons / (6 * 231.5 g) = **2.6E21 electrons**

Values in table 2 (before last column) are obtained by multiplying this result by percent of the transformed material.

2) To calculate the Se(VI) to Se(0) reduction we use the same equation, however it is true only for pH 7 series. At pH 5 we have a second reduction process.

Example:

Se(VI) , pH 7, where 1.27 mmol/L is sorbed on the mineral.

For 1 mol of Se(VI) we need 6 mole of electrons. How many electrons are needed for 1.27 mmol of Se(VI)?

x = 1.27 mmol * 6 * 6.02E23 electrons / 1000mmol = **4.59E21 electrons**

This is a value for L which contains 10 g of magnetite. To obtain the value per 1 g we need to divide it by 10.